Implementation of nuclear time-dependent density-functional theory and its application to the nuclear isovector electric dipole resonance

Yue Shi (石跃),[1,*] Nobuo Hinohara,[2,3] and Bastian Schuetrumpf[4]

[1]*Department of Physics, Harbin Institute of Technology, Harbin 150001, People's Republic of China*
[2]*Center for Computational Sciences, University of Tsukuba, Tsukuba 305-8577, Japan*
[3]*Faculty of Pure and Applied Sciences, University of Tsukuba, Tsukuba 305-8571, Japan*
[4]*GSI Helmholzzentrum für Schwerionenforschung, Planckstraße 1, 64291 Darmstadt, Germany*

(Received 16 January 2020; revised 10 September 2020; accepted 9 October 2020; published 26 October 2020)

Background: Time-dependent density-functional theory (TDDFT) continues to be useful in describing a multitude of low-energy static and dynamic properties. In particular, with recent advances of computing capabilities, large-scale TDDFT simulations are possible for fission dynamics as well as isovector dipole (IVD) resonances.
Purpose: Following a previous paper [Shi, Phys. Rev. C **98**, 014329 (2018)], we first present a time-dependent extension of the density-functional theory to allow for dynamic calculations based on the obtained static Hartree-Fock + Bardeen-Cooper-Schrieffer (BCS) results. Second, we apply the TDDFT + BCS method to a systematic description of the IVD resonances in the Zr, Mo, and Ru isotopes.
Methods: To benchmark the TDDFT code, we compute the strengths of IVD resonances for light nuclei using two complementary methods: TDDFT and FAM-QRPA methods. For the TDDFT results, additional benchmark calculations have been performed using the well-tested code Sky3D. In these three calculations, the important ingredients which have major influence on the results, such as time-odd potentials, boundary conditions, smoothing procedures, spurious peaks, etc., have been carefully examined.
Results: The current TDDFT and the Sky3D codes yield almost identical response functions once both codes use the same time-odd mean fields and absorbing boundary conditions. The strengths of the IVD resonances calculated using the TDDFT and FAM-QRPA methods agree reasonably well with the same position of the giant dipole resonance. Upon seeing a reasonable accuracy offered by the implemented code, we perform systematic TDDFT + BCS calculations for spherical Zr and Mo isotopes near $N = 50$, where experimental data exist. For neutron-rich Zr, Mo, and Ru isotopes where shape evolution exists we predict the photoabsorption cross sections based on oblate and triaxial minima.
Conclusions: The TDDFT + BCS code provides reasonable description for IVD resonances. Applying it to the spherical Zr and Mo nuclei, a reasonable agreement with experimental data has been achieved. For neutron-rich Zr isotopes, the photoabsorption cross section based on the two coexisting minima reflects the feature of the deformation of the minima. This suggests the possibility of obtaining additional information about the ground-state deformation by comparing the GDR data with the TDDFT + BCS results.

DOI: 10.1103/PhysRevC.102.044325

I. INTRODUCTION

Since its first numerical realizations in the late 1970s [1–3], the time-dependent density-functional theory (TDDFT) continues to be useful in describing a variety of low-energy nuclear static and dynamic properties, ranging from the linear response of nuclear density, to the large-amplitude motion of heavy nuclei [4–8]. The modern developments [9–11] allow for the inclusion of the full original Skyrme energy density functional (EDF) in the framework of nuclear density-functional theory (DFT). Hence, the same EDFs obtained from the knowledge of the static properties of nuclei can be applied in dynamic simulations without any further approximation.

With advances of computing capabilities, nowadays one can perform TDDFT simulations that were not possible even 20 years ago. For example, the linear-response properties of medium or heavy nuclei, fission dynamics of actinides, as well as nuclear reaction involving medium-heavy nuclei are within the reach of calculations with single-node computers.

However, computational costs to include the nuclear pairing correlation in the TDDFT dynamics is still very demanding. Several independent approaches with different treatment of the pairing have been developed. For instance, The BCS pairing [12] and Superfluid Local Density Approximation [13–15] are employed in for the time-dependent Hartree-Fock-Bogoliubov (TDHFB) simulation in the three-dimensional (3D) Cartesian coordinate space. In the linearized limit, the coordinate-basis canonical TDHFB method has been systematically applied for the low-lying diople mode [16,17]. The harmonic-oscillator (HO) and Lagrange-mesh based

*yueshi@hit.edu.cn

TDHFB calculations with finite-range Gogny force [18,19] have become available, taking advantage of the fact that the oscillation extends only in a relatively small region. The latter code is also applicable to the collision dynamics [20,21]. Recently, finite-amplitude method for quasiparticle random-phase approximation (FAM-QRPA) calculations in the 3D Cartesian coordinate space have also emerged [22].

The goal of our project is to describe low-energy large-amplitude motion such as nuclear fusion and fission using TDDFT. To this end, the 3D Cartesian coordinate space calculation with proper treatment of the dynamical nuclear pairing correlation is indispensable. Some of the earlier works [13–15] have developed these features. As a first step towards this goal, in the present work, we show an extension of an earlier developed Skyrme-HFB code [23] on time-dependent capabilities with fixed-occupation probabilities [24,25]. The code is represented in the 3D Cartesian coordinate space, using a light-weighted finite-difference method for derivative operators. The code features an interface with the HFODD code [26–28], which is a Skyrme-Hartree-Fock-Bogoliubov (HFB) code in a 3D HO basis. Such a flexible code is desired to provide a reasonable alternative for future development.

As the first application, the current work provides systematic calculations for the isovector (IV) electric dipole ($E1$) vibration motion for stable and neutron-rich Zr, Mo, and Ru isotopes. Although there exist a few systematic calculations for IV and isoscalar vibrational properties for nuclei across the nuclear chart [17,29–31], we find that a detailed analysis of the shape evolutions and shape coexistence in the same nucleus, reflected by the different structures of the GDR cross sections, is particularly useful [32].

In Sec. II we present a description about the main features of the current TDDFT + BCS framework. Section III contains two parts: first, a set of careful benchmark calculations, with the current TDDFT, Sky3D codes, and the FAM-QRPA calculations, have been presented. Second, systematic calculations have been performed for the photoabsorption cross section of the isovector dipole (IVD) vibration in the spherical and deformed Zr, Mo, and Ru nuclei. A summary is contained in Sec. IV.

II. THE MODEL

This section describes in detail the procedure for the time development in connection with the previous static calculation [23]. Then, we briefly describe the Sky3D [24,25] calculation, with which the current code is benchmarked. For the applications in the linearized limit of the current TDDFT calculation, we provide formulas for describing the relevant properties associated with the $E1$ vibrational mode.

A. The static calculations

Before the single-particle wave functions are propagated in time, one has to obtain the static solution of the Hartree-Fock (HF) problem. In this stage of the calculation, the time-odd components of the densities and mean-fields vanish for even-even nuclei. The form of the Hamiltonian, the way how the operators of the Hamiltonian are constructed, and how the integrations are performed have been explained in Ref. [23].

1. The grid points arrangement

The grid points in the present implementation are moved away from the origin of the simulating box and differs from those of Ref. [23]. Specifically, in the example of one dimension, instead of using a set of coordinates at

$$[-nx_{\max}, \ldots, 0, 1, \ldots + nx_{\max}] \times dx, \tag{1}$$

the current code represents the problem on grid points at the coordinates

$$[-nx_{\max} + 0.5, \ldots, -0.5, 0.5, \ldots + nx_{\max} - 0.5] \times dx, \tag{2}$$

where $nx_{\max}$ is an integer number numerating the points at the edge of the simulating box. The dx denotes the grid spacing. Note, that the latter choice has an even number of grid points, whereas the former one has an odd number of grid points. This choice is guided by the fact that the inclusion of the grid point at the origin of the box results in numerical problems [24]. Using the grid shown in Eq. (2), the integration can be carried out by summation *on* the grid, without the interpolation as presented in Ref. [23].

2. The Bardeen-Cooper-Schrieffer (BCS) pairing

To demonstrate the influence of the pairing interaction on the properties of the IVD resonances, we include a simple BCS pairing [33–35]. For the BCS method, we attach each single-particle wave function a real number, v_i, whose square gives the occupation probability of the ith orbit.

After each HF iteration, the occupation amplitude v_i is determined, in the current work, by the following BCS equations

$$v_{i,q}^2 = \frac{1}{2}\left[1 - \frac{\epsilon_{i,q} - \lambda_q}{\sqrt{(\epsilon_{i,q} - \lambda_q)^2 + \Delta_{i,q}^2}}\right], \tag{3}$$

where $\epsilon_{i,q}$'s are the HF single-particle energies; λ_q is the Fermi energy for given nucleonic type, which is adjusted so that $2\sum_i v_{i,q}^2$ gives the correct nucleon number. In Eq. (3), the state-dependent single-particle pairing gaps, $\Delta_{i,q}$'s, are given by

$$\Delta_{i,q} = \sum_\sigma \int d\boldsymbol{r} \Delta_q(\boldsymbol{r}) \psi_{i,q}^*(\boldsymbol{r}, \sigma) \psi_{i,q}(\boldsymbol{r}, \sigma), \tag{4}$$

where

$$\Delta_q(\boldsymbol{r}) = -\frac{1}{2} V_q \int d\boldsymbol{r}\left[1 - \frac{\rho(\boldsymbol{r})}{\rho_{\text{pair}}}\right]\tilde{\rho}_q(\boldsymbol{r}), \tag{5}$$

$$\rho_q(\boldsymbol{r}) = \sum_{i,\sigma} v_{i,q}^2 \, \psi_{i,q}^*(\boldsymbol{r}, \sigma) \psi_{i,q}(\boldsymbol{r}, \sigma), \tag{6}$$

$$\tilde{\rho}_q(\boldsymbol{r}) = \sum_{i,\sigma} v_{i,q} \sqrt{1 - v_{i,q}^2} \, \psi_{i,q}^*(\boldsymbol{r}, \sigma) \psi_{i,q}(\boldsymbol{r}, \sigma), \tag{7}$$

with $q = n, p$ denoting the neutron and proton, respectively. The quantities without subscripts denote the summed

contributions from neutrons and protons, for example, $\rho = \rho_n + \rho_p$. We choose $\rho_{\rm pair} = 0.32\ {\rm fm}^{-3}$ in this work.

When applied to the drip-line nuclei, using the BCS pairing tends to scatter the particles to the positive-energy levels which are nonlocal, resulting in the unphysical nucleon gas surrounding the nucleus. This problem can be cured by replacing the BCS theory with the HFB theory [36]. In the current work, we limit the TDDFT+BCS calculations to the nuclei far from drip line. This indicates that the Fermi surfaces are far from the positive-energy level. Hence, these orbits are less occupied compared to those bound orbits. Among the nuclei studied in the current work, the most neutron-rich one is ^{34}Mg, where the most significant occupation probability of the positive-energy level is in the order of 10^{-5}, which is three orders of magnitude smaller than the probability of the least occupied bound state. It has been checked that the neutron densities for paired ^{34}Mg would decrease exponentially with the increase of the distance from the center of the nucleus. Hence, this small occupation would not lead to the nucleon gas problem in the neutron density distribution. For the neutron-rich Zr, Mo, and Ru isotopes, the largest occupation of the scattering state is also in the order of 10^{-5}, for the paired calculation shown in Sec. III B.

B. The nuclear mean fields including the time-odd parts

In the earlier static code presented in Ref. [23], it has been explained that the time-odd densities and mean fields vanish due to the time-reversal symmetry. When time propagation is discussed, the time-odd densities and mean fields appear [1]. Due to computing limitations, historically, the earlier TDHF calculations contained a few serious approximations such as the schematic treatment of the spin-orbit and pairing interactions. Modern TDHF calculations [9–11] include the full Skyrme interactions. Recent studies discuss the influence of the tensor interactions when applied to the description of GDR [37] and nuclear collisions [38].

The current paper adopts the frequently used Skyrme EDF which contains, in addition to the time-even densities, time-odd densities $\boldsymbol{s}$ and $\boldsymbol{j}$. The tensor interaction is not considered in this work. See Eq. (A.19) of Ref. [1] for a detailed form of the Skyrme energy density $\mathcal{H}(\boldsymbol{r})$.

After variation of the total energy, $E = \int \mathcal{H}(\boldsymbol{r})d\boldsymbol{r}$, with respect to the density matrix, the resulting Skyrme mean fields also contain terms of the above-mentioned time-odd densities. Modern nuclear DFT allows for a free parametrization of coupling constants in front of each term in the Skyrme mean field. See Eq. (2.6) of Ref. [39] for details. Assuming local gauge invariance of the energy density, one requires the terms contributing to the mean fields to be grouped in pairs [39], specifically, $(\rho\tau - \boldsymbol{j}^2)$ and $(\rho\boldsymbol{\nabla}\cdot\boldsymbol{J} + \boldsymbol{s}\cdot\boldsymbol{\nabla}\times\boldsymbol{j})$.

In the current implementation of the TDDFT code, the single-particle Hamiltonian reads

$$\hat{h}_q = -\boldsymbol{\nabla}\cdot\frac{\hbar^2}{2m^*}\boldsymbol{\nabla} + U_q - i\boldsymbol{B}_q\cdot(\boldsymbol{\nabla}\times\boldsymbol{\sigma}) + \boldsymbol{\sigma}\cdot\boldsymbol{\Sigma}_q + \frac{1}{2i}(\boldsymbol{\nabla}\cdot\boldsymbol{I}_q + \boldsymbol{I}_q\cdot\boldsymbol{\nabla}). \tag{8}$$

For protons, one needs to add Coulomb potentials (Eqs. (20) and (24) in Ref. [23]). The detailed expression of U_q can be found in Eq. (18) of Ref. [23]. The time-odd potentials included in Eq. (8) read

$$\boldsymbol{\Sigma}_q = \tfrac{1}{3}(-b_0 + 2b_0')\boldsymbol{s} - \tfrac{1}{3}(2b_0 - b_0')\boldsymbol{s}_q - b_4\boldsymbol{\nabla}\times\boldsymbol{j} - b_4'\boldsymbol{\nabla}\times\boldsymbol{j}_q, \tag{9}$$

$$\boldsymbol{I}_q = -2b_1\boldsymbol{j} + 2b_1'\boldsymbol{j}_q - b_4\boldsymbol{\nabla}\times\boldsymbol{s} - b_4'\boldsymbol{\nabla}\times\boldsymbol{s}_q. \tag{10}$$

In the current work, those terms containing $\Delta\boldsymbol{s}$ are ignored. This is because, frequently, the inclusion of the $\Delta\boldsymbol{s}$ and $\boldsymbol{\nabla}\cdot\boldsymbol{s}$ terms is known to induce the finite-size instabilities [40]. Hence, it has been the common practice for the time-dependent applications of the DFT to ignore these terms, see Ref. [41] for instance.

C. Time propagation

The nuclear nonrelativistic time-dependent Schrödinger equation reads

$$i\hbar\frac{\partial\psi_{i,q}(t)}{\partial t} = \hat{h}_q(t)\psi_{i,q}(t), \tag{11}$$

where $\hat{h}_q$ can be found in Eq. (8). In this section, the subscript q is ignored for simplicity. Equation (11) has the formal solution

$$\psi_i(t) = \hat{\mathscr{U}}(t)\psi_i(0) = \hat{T}\exp\left(-\frac{i}{\hbar}\int_0^t \hat{h}(t')\,dt'\right)\psi_i(0), \tag{12}$$

where $\hat{\mathscr{U}}$ is the time-evolution operator, and $\hat{T}$ is the time-ordering operator. To solve the time-dependent problem, one breaks up the total time evolution into N small increments of time Δt,

$$\hat{U}(t, t+\Delta t) = \exp\left(-\frac{i}{\hbar}\int_t^{t+\Delta t}\hat{h}(t')\,dt'\right). \tag{13}$$

The time-evolution operator $\hat{\mathscr{U}}(t)$ can be obtained by consecutive actions of $\hat{U}(t, t+\Delta t)$,

$$\hat{\mathscr{U}}(t) = \prod_{n=0}^{N-1}\hat{U}(n\Delta t, (n+1)\Delta t). \tag{14}$$

For small Δt one could approximate $\hat{U}(t, t+\Delta t)$ by Taylor expansion up to order m:

$$\exp\left(-\frac{i}{\hbar}\hat{h}\Delta t\right) \approx \sum_{n=0}^{m}\frac{1}{n!}\left(\frac{-i\Delta t}{\hbar}\right)^n\hat{h}^n, \tag{15}$$

where $\hat{h}$ has been assumed to be time independent in the time interval of Δt. In the current work, Δt is taken to be 0.2 fm/c, and $m = 4$. These choices are motivated by previous TDHF calculations.

In the realistic calculations, each time advance of single-particle wave functions ψ_i, from time t to $t + \Delta t$, has been achieved by using the Crank-Nicolson method [2]. Specifically, from a series of single-particle wave functions at t, $\psi_i(t)$, one first performs

$$\psi_i^{\rm temp}(t+\Delta t) = \hat{U}^{\rm t}(t, t+\Delta t)\psi_i(t). \tag{16}$$

Having $\psi_i^{\rm temp}(t+\Delta t)$, and $\psi_i(t)$, one assembles various densities using respective single-particle wave functions, obtaining the $\rho^{\rm temp}(t+\Delta t)$ and $\rho(t)$.

Using these densities, one obtains the densities at a "middle time", $\rho^{\rm mid}(t+\frac{\Delta t}{2}) = 0.5[\rho^{\rm temp}(t+\Delta t)+\rho(t)]$. Now, one constructs the Hamiltonian $\hat{h}^{\rm mid}$, using $\rho^{\rm mid}(t+\frac{\Delta t}{2})$ [see Eq. (15) of Ref. [23], and Eq. (8) for the form of the Hamiltonian]. A second time propagation operation $\hat{U}^{\rm mid}(t, t+\Delta t)$ with $\hat{h}^{\rm mid}$ [Eq. (15)] is performed on the single-particle levels, finally obtaining the wave functions at $t+\Delta t$,

$$\psi_i(t+\Delta t) = \hat{U}^{\rm mid}(t, t+\Delta t)\psi_i(t). \tag{17}$$

Here, $\hat{U}^{\rm mid}$ differs from $\hat{U}^{\rm t}$ [Eq. (16)] in that the former uses the single-particle Hamiltonian in its exponent [Eq. (15)] at the time $t+\frac{\Delta t}{2}$, whereas the latter refers to the operator $\hat{U}$, where the Hamiltonian is constructed using the quantities at the time t.

Note that in the above procedure, one has to perform the time propagation twice. The single-particle Hamiltonian does not contain time specifically. In realistic calculations, the unitarity of the operator $\exp(-\frac{i}{\hbar}\hat{h}\Delta t)$ needs to be checked as it is approximated using a Taylor expansion [Eq. (15)]. For the chosen parameter, $\Delta t = 0.2$ fm/c and $m = 4$, we evaluate the matrix elements

$$\mathcal{I}_{ij} \equiv \langle\psi_i(t)|\hat{U}|\psi_j(t)\rangle \approx \langle\psi_i(t)|\psi_j(t+\Delta t)\rangle. \tag{18}$$

Both the diagonal and off-diagonal matrix elements start to deviate from 1 and 0, respectively, at or after the 6th place after the decimal point. For a better approximation of the $\hat{U}$ operator, one could decrease Δt and increase m.

When the BCS pairing is included, the occupation amplitudes, $v_{i,q}$'s in Eq. (3), are kept unchanged when calculating the densities during the time development [24,25]. When evaluating the densities, the single-particle wave functions vary according to Eq. (11). This is a coarse approximation of dynamical pairing, as the occupation probabilities should vary with time. Indeed, some of the problems associated with the TDHF + BCS method in describing particle transport has been discussed in Ref. [42]. This approximation of the pairing will be improved in our future publications. A natural extension would be to solve the full time-dependent HFB problem [13–15]. Since the HFB theory treats nuclear interactions in the particle-hole and pairing channels in one single variational process [34], a time-dependent HFB treatment allows for the occupation amplitudes being determined dynamically by the upper and lower components at a given time.

D. Absorbing boundary conditions (ABC)

With Dirichlet boundary conditions, it has been known that the TDDFT calculations show the occurrence of nonphysical particle densities at the boundary region. To cure this problem, it has been proposed [9] to use the so-called absorbing boundary conditions. This is achieved by introducing an imaginary potential,

$$\hat{h}(\boldsymbol{r}) \to \hat{h}(\boldsymbol{r}) + i\tilde{\eta}(\boldsymbol{r}), \tag{19a}$$

at the boundary region of the form

$$\tilde{\eta}(\boldsymbol{r}) = \begin{cases} 0 & \text{for } 0 < |\boldsymbol{r}| \leqslant R \\ \eta_0 \frac{|\boldsymbol{r}|-R}{\Delta r} & \text{for } R < |\boldsymbol{r}| < R+\Delta r \end{cases}. \tag{19b}$$

Recently, there have been efforts using more involved boundary conditions [43,44]. Based on these studies, we decide to use the ABC due to its simplicity and effectiveness.

E. IVD resonance calculations

The IVD resonance is the most common vibrational mode in nuclear physics, where neutrons and protons vibrate against each other. This mode is responsible for the $E1$ resonant strengths in the energy range of ∼10–20 MeV. This broad peak is called giant dipole resonance (GDR) [45]. The current work aims at a description of the IVD resonance in terms of the TDDFT in its linearized limit, which is equivalent to the random-phase approximation (RPA) [34].

In the TDDFT description, the strength of this IVD vibrational mode can be obtained by applying the following small boost on the obtained single-particle wave functions,

$$\psi_{i,q}(\boldsymbol{r},\sigma;t=0+) \equiv \exp\left[-i\epsilon\sum_{\mu=-1}^{+1}\mathcal{M}(E1,\mu)\right]\psi_{i,q}(\boldsymbol{r},\sigma), \tag{20}$$

with the IV operator $\mathcal{M}(E1,\mu)$ defined as

$$\mathcal{M}(E1,\mu) = e_q^{(E1)} r Y_{1\mu}(\hat{\mathbf{r}}) \qquad \mu = 0,\pm 1, \tag{21}$$

where $e_p^{(E1)} = Ne/A$, and $e_n^{(E1)} = -Ze/A$. When $\mathcal{M}(E1,\mu)$ acts on neutron/proton single-particle wave functions, its coefficient takes value of $e_p^{(E1)}/e_n^{(E1)}$. The real spherical harmonics are defined as

$$\{Y_{1\mu}\}_{\mu=-1,0,1} = \left\{\sqrt{\frac{3}{4\pi}}\frac{\lambda}{r}\right\}_{\lambda=y,z,x}. \tag{22}$$

In Eq. (20), the boosted single-particle wave functions differ from the static ones by including "$t = 0+$", indicating their time-dependency. This IV boost has to be small enough to ensure that the vibration is still within the linearized regime. The typical magnitude of $|\epsilon|$ is 10^{-3} $(e\,\text{fm})^{-1}$. In this work, we apply 3D boost which has been indicated by the summation over μ in the exponent in Eq. (20). For nonspherical nuclei, the 3D boost allows for obtaining the moments along the three axes in a single run. The boost is applied over the whole box, although a masking procedure works better confining its effect in the range of the nucleus [46].

The time evolution of the dipole moment

$$\langle\mathcal{M}(E1,\mu)\rangle \equiv \int e_n^{(E1)}\rho_n r Y_{1\mu}d\boldsymbol{r} + \int e_p^{(E1)}\rho_p r Y_{1\mu}d\boldsymbol{r} \tag{23}$$

is then recorded to certain length of time. Note, that although the boost is 3D, the resulted $\langle\mathcal{M}(E1,\mu)\rangle$ are extracted for each K component without summing them. The strengths are the Fourier transform of $\langle\mathcal{M}(E1,\mu)\rangle(t)$,

$$S(E;E1) = -\frac{1}{\pi\hbar\epsilon}\text{Im}\sum_{\mu=-1}^{+1}\int\langle\mathcal{M}(E1,\mu)\rangle(t)\,dt\,e^{(iE-\Gamma/2)t/\hbar}, \tag{24}$$

where Γ is a smoothing parameter. The photoabsorption cross section associated with the IVD resonance is obtained as follows [34]:

$$\sigma_{\text{abs.}} = \frac{16\pi^3}{9\hbar c} E \times S(E;E1). \tag{25}$$

For a nucleus localized in space, the translational symmetry is spontaneously broken. This results in the existence of the spurious excitation of center-of-mass modes in the self-consistent calculations. For a perfect IVD vibrational calculation, however, these spurious modes cannot be excited as they are completely decoupled with the IVD mode. In realistic calculations, due to the finite size of the basis one is working, the spurious mode may appear at finite excitation energy and may be mixed among the physical IVD excitations. The current work based on a finite-difference representation for the TDDFT + BCS code and the HO basis for the FAM QRPA code uses the IVD modes and we do not see a prominent spurious peak with this operator. Thus in this work, the mixture of the spurious modes in the IVD modes is expected to be small.

F. Calculation of energy-weighted sum rule (EWSR) for the IVD vibration

Another important aspect of the vibration calculations is the evaluation of EWSR [34], which is a useful check of the implementation of the TDDFT code. In the TDDFT code, the sum rule is calculated using

$$m_1 = \int E \times S(E;E1) dE. \tag{26}$$

Recently, the EWSR for the density-functional theory has been systematically derived in Refs. [47,48]. For the current IVD operator, the sum rule using Eq. (98) of Ref. [48] can be adapted as follows:

$$\begin{aligned} m_1 = \sum_{\mu=-1}^{+1} \int d\boldsymbol{r} [\nabla (r Y_{1\mu})]^2 \Bigg\{ & \frac{\hbar^2}{2m} \left[e_n^{(E1)^2} \rho_n + e_p^{(E1)^2} \rho_p \right] \\ & + \left(C_0^\tau - C_1^\tau \right) \left(e_n^{(E1)} + e_p^{(E1)} \right)^2 \rho_n \rho_p \\ & + \sum_{k=0,1} \left(C_k^\tau + C_k^j \right) \left[e_n^{(E1)} \rho_n + (-1)^{k+1} e_p^{(E1)} \rho_p \right]^2 \Bigg\}. \end{aligned} \tag{27}$$

The definition of the spherical harmonics can be found in Eq. (21). The coupling constants in terms of $C_{0,1}^{\tau,j}$ are related to b_1, b_1' through

$$C_0^\tau = -C_0^j = b_1 - 0.5 b_1', \tag{28}$$

$$C_1^\tau = -C_1^j = -0.5 b_1'. \tag{29}$$

If we define the kinetic-energy contribution

$$\begin{aligned} m_1^{\text{kin}} &= \sum_{\mu=-1}^{+1} \int d\boldsymbol{r} [\nabla (r Y_{1\mu})]^2 \frac{\hbar^2}{2m} \left[e_n^{(E1)^2} \rho_n + e_p^{(E1)^2} \rho_p \right] \\ &= \frac{9}{4\pi} \frac{\hbar^2}{2m} \frac{NZ}{A} e^2, \end{aligned} \tag{30}$$

then the enhancement factor, κ, due to the contribution of interaction-energy term with respect to the kinetic part, can be calculated through

$$m_1 = m_1^{\text{kin}} (1 + \kappa). \tag{31}$$

The classical sum rule of the IVD operator, which is the Thomas-Reiche-Kuhn (TRK) sum rule [49] can be analytically expressed as shown in Eq. (30).

The EWSR value obtained from Eq. (27) are related to various densities of the ground state. Thus, they can be determined rather precisely. To what extent the m_1 values obtained from TDDFT [Eq. (26)] and Eq. (27) agree, forms a stringent testing ground for the TDDFT code.

G. Sky3D calculations

To demonstrate the precision of the current code, it is necessary to benchmark it against an existing code with an identical calculation. In this work, this benchmark is done with a well-established code Sky3D.

We use the Sky3D code as described in Refs. [24,25]. An important difference to the implementation presented in this code is that derivatives are performed utilizing the fast Fourier transform and thus the natural boundary conditions are periodic boundary conditions. The difference is of special importance for time-dependent calculations, as it affects the quantization of unbound energy states. Furthermore, when evaporated material is leaving the box it is again introduced from the other side of the box and not reflected as with Dirichlet boundary conditions. The codes differ slightly in the way the density at middle time is approximated. In Sky3D the wave functions are propagated until middle time $t + \Delta t/2$. These densities are then directly taken to calculate the Hamiltonian at middle time $\hat{h}^{\text{mid}}$.

For the benchmarks we implemented the same boost as described in Sec. II E and also the imaginary potential for the ABC from Sec. II D.

III. RESULTS AND DISCUSSIONS

To complete the benchmark of the implemented TDDFT code, one has to include careful calculations and compare the calculated results with those of existing codes. Particularly useful testing cases for the TDDFT code are the calculations of IVD resonance for light spherical and deformed nuclei.

In Ref. [9] careful comparative study has been done between the TDDFT code and the RPA calculations. Detailed dipole-moment response as a function of time, as well as the corresponding strengths results for ^{16}O nucleus has been presented with the specific force being provided. In this section, we first present results of the current code, comparing them with those of Sky3D code and Ref. [9]. The calculation is then extended to a spherical nucleus ^{40}Ca, as well as deformed magnesium isotopes ^{24,34}Mg with conventional Skyrme EDF SkM* [50], and a more recent EDF UNEDF1 [51].

The UNEDF1 EDF contains Lipkin-Nogami (LN) pairing [51] in the parameter adjustment process. In principle, one has to include this part specifically. However, we decide to be more flexible in the pairing treatment for the current TDDFT

calculations based on the two following considerations. First, the original UNEDF1 parameter is determined in the HO basis and with specific cutoff on the HFB problem. Whereas the current code is working in the 3D Cartesian coordinate space. Hence, the continuum is discretized differently from that of a HO code. Consequently, there is no way to make the pairing treatment identical in the two codes [23]. Second, the observables we are interested in, namely, the strengths for the IVD resonances are well known to be insensitive to the pairing interactions [52]. The strengths corresponding to pygmy dipole resonance (PDR) are only enhanced very marginally by including the pairing interaction, as will be shown in Sec. III A 3.

A. Results for light nuclei

1. Benchmark calculations for ^{16}O with Skyrme SIII EDF

The nucleus ^{16}O is of particular interest in theoretical benchmarking calculations, as the structure of the strength is sensitive to the included terms in the EDF [9]. Hence, many theoretical methods [37,53,54] took ^{16}O as a testing case for the proposed method. In this section, we perform TDDFT calculations with Skyrme force parameter SIII [55] with time-odd potentials in the form of Eq. (9) (SIII-full), as well as SIII without any time-odd contributions (SIII-even). For the calculations presented in Fig 1, the time-odd potentials are identical with that of the Sky3D code [Eqs. (8e) and (8f) of Ref. [24]]. Specifically, the time-odd potentials are the same as SIII-full, except that the terms including *only* $\boldsymbol{s}$ are left out.

Figure 1 displays a set of comparisons of responses of the dipole moments between the currently implemented code and the Sky3D code. Figure 1(a) compares the response functions without any absorbing mechanism. We see that the magnitude agrees well for $t \leqslant 400$ fm/c. However, the good agreement starts to deteriorate after $t \approx 500$ fm/c. This is due to the different boundary conditions used in the two codes, which results in the different treatment of the particle densities bounced back from the border of the box. Indeed, even within the same code, using a finer grid results in rather different response functions after certain time.

Figure 1(b) compares the response functions with the ABC [Eq. (19)] calculated with both codes. For both codes we use $\eta_0 = 10$ MeV, $R = 10$ fm, and $\Delta r = 12$ fm. It can be seen that with the same ABC, both codes give almost identical response functions. The difference of the dipole moment, shown in the inset, is at least an order of magnitude smaller than the original moment value. Fig. 1(c) shows the photoabsorption cross sections calculated from the response functions shown in Fig. 1(b). Again, the agreement is remarkable.

Figure 2 shows the calculated photoabsorption cross sections for SIII-full and SIII-even, with $\Gamma = 0.5$ MeV and without the smoothing procedure ($\Gamma = 0$). Again, a good correspondence can be seen between Fig. 6(b) of Ref. [9] and Fig. 2 of the current work. Specifically, for SIII-full we see, for both results, that the single largest peak occurs at $E \approx 21.2$ MeV. For SIII-even, the two peaks occur at $E \approx 19.4$ and 21.8 MeV for both the current result and those shown in Fig. 6(b) of Ref. [9]. Using a smoothing parameter of

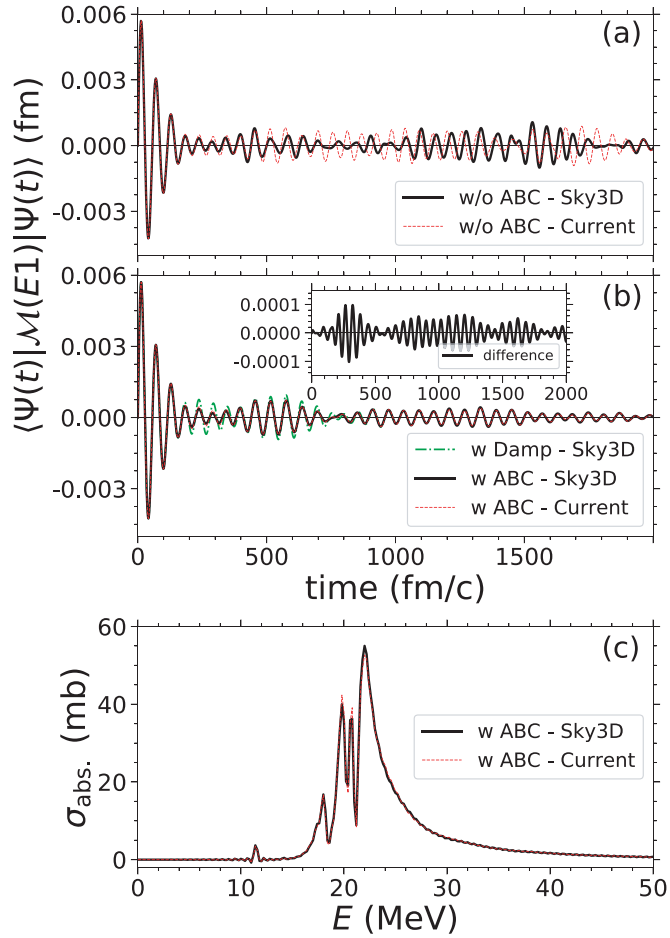

FIG. 1. The response functions, $\langle \mathcal{M}(E1, \mu = 0)\rangle(t)$, of ^{16}O calculated with the current TDDFT code and the Sky3D code [24]. The inset of panel (b) shows the difference between the $\langle \mathcal{M}(E1, \mu = 0)\rangle$ values calcualted with the TDDFT and the Sky3D codes, both including the ABC. The panel (c) shows the cross sections resulted from the respective response functions in the panel (b). The smoothing parameter is $\Gamma = 0$.

$\Gamma = 0.5$ MeV brings the general energy dependence of the photoabsorption cross sections rather close to those given in Fig. 6(b) of Ref. [9].

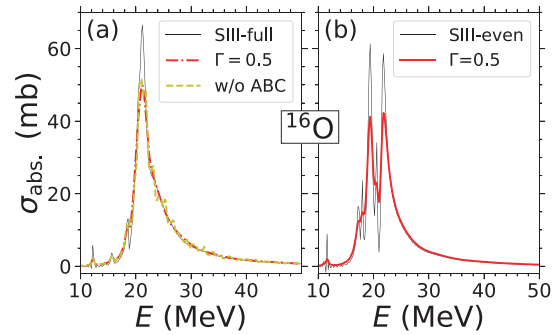

FIG. 2. The calculated photoabsorption cross sections of ^{16}O using Eq. (25). The left panel shows the results with SIII-full EDF, whereas the right panel shows those with SIII-even. The thinner black lines indicate the results without smoothing procedure.

TABLE I. The calculated static properties for ^{16}O and ^{40}Ca with UNEDF1 EDF, using the current TDDFT and the HFBTHO codes. For the TDDFT calculations, the simulation boxes have dimensions of $[-14.5, +14.5]^3$ fm^3. Three grid spacings have been used to see the convergence of the TDDFT calculations. For the HFBTHO calculations, 20 HO shells are used.

	^{16}O				^{40}Ca			
	Current			HFBTHO	Current			HFBTHO
	$\Delta x = 1.0$ fm	$\Delta x = 0.784$ fm	$\Delta x = 0.707$ fm		$\Delta x = 1.0$ fm	$\Delta x = 0.784$ fm	$\Delta x = 0.707$ fm	
$E_{\rm tot}$ (MeV)	−121.139	−120.997	−120.986	−121.000	−340.873	−340.599	−340.571	−340.625
$E_{\rm Kin.}$ (MeV)	236.905	236.443	236.414	236.494	659.414	658.387	658.290	658.505
E_{ρ} (MeV)	−406.666	−405.978	−405.936	−406.055	−1137.525	−1135.918	−1135.749	−1136.071
E_{τ} (MeV)	−0.890	−0.886	−0.886	−0.886	−3.218	−3.209	−3.207	−3.209
$E_{\Delta\rho}$ (MeV)	36.522	36.486	36.492	36.520	68.788	68.601	68.575	68.640
$E_{\rm SO}$ (MeV)	−0.636	−0.671	−0.677	−0.681	−0.979	−1.046	−1.059	−1.077
$E^{\rm Coul.}_{\rm dir.}$ (MeV)	16.448	16.429	16.427	16.428	80.201	80.132	80.124	80.134
$E^{\rm Coul.}_{\rm exc.}$ (MeV)	−2.823	−2.820	−2.820	−2.820	−7.554	−7.547	−7.546	−7.548
$r^{\nu}_{\rm rms}$ (fm)	2.666	2.669	2.669	2.668	3.360	3.362	3.362	3.362
$r^{\pi}_{\rm rms}$ (fm)	2.684	2.687	2.687	2.686	3.395	3.398	3.398	3.398
$r^{\rm tot.}_{\rm rms}$ (fm)	2.675	2.678	2.678	2.677	3.377	3.380	3.380	3.380

In these calculations, we use the ABC as described in Sec. II D. In Fig. 2(a), we also include the results without the ABC. It can be seen that the strength without the ABC differs from that with the ABC in that the former gives small peaks for excitation energies larger than that corresponds to the main peak. These small peaks are spurious which are removed by absorbing potential in the outer layer region.

2. *Comparing TDDFT with FAM-RPA:* ^{16}O *and* ^{40}Ca

In this section, we compare our TDDFT approach to the RPA calculation based on the linear-response formalism, the finite-amplitude method (FAM) [56,57]. The FAM allows us to calculate the response function without constructing the QRPA matrices in the case of the nuclear DFT. The present implementation of the FAM-QRPA [58] is based on the nuclear DFT solver HFBTHO [59–61], which allows to describe the superconducting axially deformed nuclei in the HO basis.

Before showing the cross-section results, we first present the calculated static properties using both codes. Table I lists the calculated ground-state energy decomposition into various terms, as well as the root-mean-square radii. For a fixed box size, three different grid spacings have been used. It can be seen that the ground-state energy is overbound by <200 keV using the coarsest grid with $dx = 1.0$ fm. Using finer grid spacings reduces the total energy differences to $\leqslant$50 keV. It should be noted that, the seemingly poor accuracy of a spacing of 1.0 fm does not drastically affect the dynamic calculation [see Fig. 1(b)].

Figure 3 shows the photoabsorption cross sections for ^{16}O and ^{40}Ca calculated with the TDDFT and FAM-RPA. The energy of the main peak and the low-energy side of the main peak agree well between the two approaches, while the high-energy tail part is more fragmented in the FAM-RPA strength. This behavior found in the calculation using the HO basis is also found in the QRPA calculations in deformed nuclei using the HO basis [62,63].

Figure 4 displays the FAM-RPA results with increasing number of HO basis ($N_{\rm sh}$). We see that the peak at $E \approx 25-35$ MeV moves toward the main peak with increasing $N_{\rm sh}$. We note a slow convergence of the strength function for this nucleus with this particular EDF. For medium-heavy nuclei, the isoscalar and isovector multipole strength functions are found to be converged already at $N_{\rm sh} = 20$ [64,65].

3. *Results for deformed nuclei:* ^{24,34}Mg

The nucleus ^{24}Mg is one of the lightest nuclei with large prolate deformation. Hence, the IVD vibration motion of this nucleus has been frequently used as a testing case for TDDFT or RPA codes. Another interesting system that has a prolately deformed ground state is ^{34}Mg. The occurrence of nonzero strength below $E = 10$ MeV in ^{34}Mg is a signature of the pygmy mode for neutron-rich Mg isotopes [16]. For neutrons, there is a pairing correlation which makes ^{34}Mg particularly interesting. In this section, we focus on the description of ^{24,34}Mg with both TDDFT and the FAM-QRPA methods.

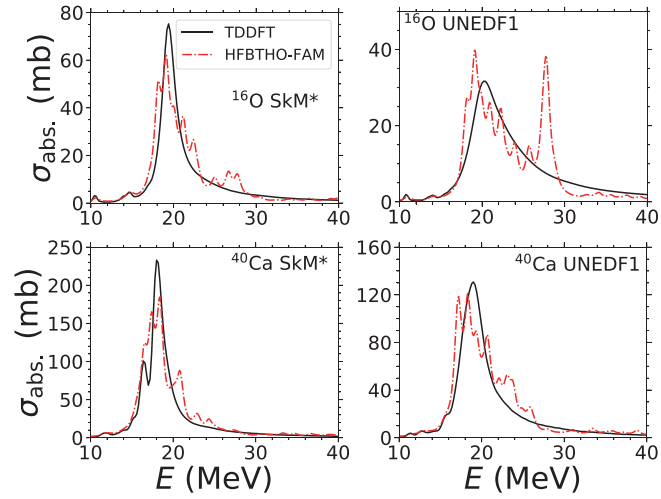

FIG. 3. The calculated photoabsorption cross sections for ^{16}O and ^{40}Ca, using TDDFT of the present implementation and FAM-RPA based on the HFBTHO with the SkM* and UNEDF1 EDFs.

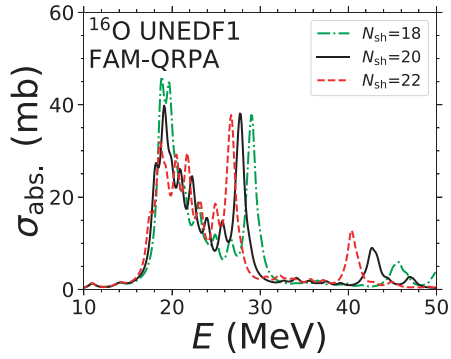

FIG. 4. The calculated photoabsorption cross sections for ^{16}O, using FAM-RPA method based on the HFBTHO with the UNEDF1 EDF. Three different HO basis numbers are used to see the convergence of the results.

Table II lists the calculated static information on ^{24}Mg with SkM* and UNEDF1 EDFs. Figure 5 plots the IV densities, $\rho_p(\mathbf{r}) - \rho_n(\mathbf{r})$, on the $x-z$ plane with $y=0$, at a few instances. As the neutrons and protons vibrate against each other, a fading and strengthening pattern of the color can be seen. Careful examination reveals the left-right and up-down asymmetry, which is due to the 3D boost that has been initiated in the current calculations.

TABLE II. Calculated static DFT results for ^{24}Mg using SkM* and UNEDF1 EDFs. A comparison is made between the results using the current TDDFT and the HFBTHO codes [59,60]. There is no center-of-mass correction for UNEDF1 calculations. The quadrupole moments are defined as $Q_{20} = 2\langle\hat{z}^2\rangle - \langle\hat{x}^2\rangle - \langle\hat{y}^2\rangle$. The single-particle levels are doubly degenerate and labeled by Ω^{parity}, where Ω denotes the total angular momentum of the level projected onto the z-axis. All quantities are in units of MeV, except for Q_{20} values which are in barn.

	SkM*		UNEDF1	
	Current	HFBTHO	Current	HFBTHO
E_{tot}	−197.123	−197.155	−189.881	−189.852
$E_{\text{Kin.+c.m.}}$	384.483	384.091	401.148	400.387
E_{Coul}	28.681	28.650	28.713	28.671
E_{Skyrme}	−610.287	−609.896	−619.742	−618.910
Q_{20}	1.072	1.072	1.126	1.137
$\epsilon^{\pi}_{1/2^+}$	−34.236	−34.249	−29.474	−29.480
$\epsilon^{\pi}_{1/2^-}$	−23.510	−23.528	−20.865	−20.898
$\epsilon^{\pi}_{3/2^-}$	−19.429	−19.396	−17.348	−17.285
$\epsilon^{\pi}_{1/2^-}$	−13.945	−13.973	−13.219	−13.196
$\epsilon^{\pi}_{1/2^+}$	−12.066	−12.075	−11.036	−11.064
$\epsilon^{\pi}_{3/2^+}$	−9.525	−9.519	−8.596	−8.585
$\epsilon^{\nu}_{1/2^+}$	−39.279	−39.290	−34.215	−34.218
$\epsilon^{\nu}_{1/2^-}$	−28.361	−28.377	−25.500	−25.529
$\epsilon^{\nu}_{3/2^-}$	−24.274	−24.235	−22.034	−21.964
$\epsilon^{\nu}_{1/2^-}$	−18.667	−18.694	−17.833	−17.806
$\epsilon^{\nu}_{1/2^+}$	−16.725	−16.729	−15.604	−15.626
$\epsilon^{\nu}_{3/2^+}$	−14.141	−14.131	−13.148	−13.132

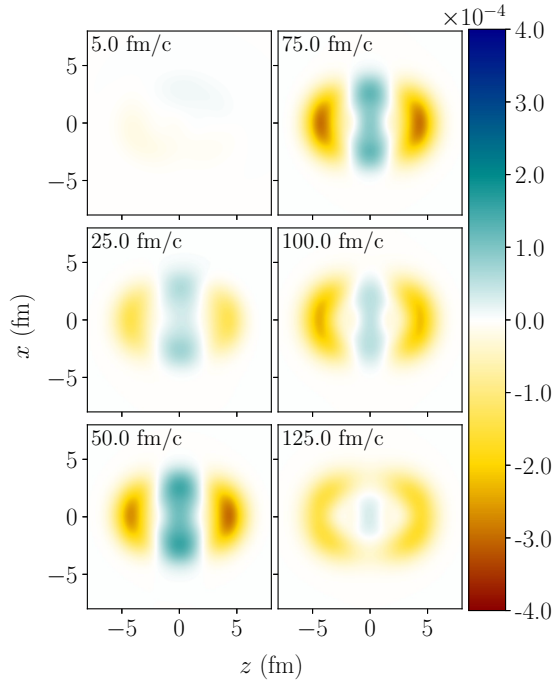

FIG. 5. Time evolution of the IV density $\rho_p(\mathbf{r}) - \rho_n(\mathbf{r})$ (in fm^{-3}) in the $x-z$ plane ($y=0$) for the IVD mode in ^{24}Mg.

Figure 6 compares the strengths calculated with SkM* and UNEDF1 EDFs. It can be seen that the two peaks calculated with UNEDF1 EDF are considerably lower and broader compared to those calculated with SkM* EDF. The positions of the two peaks are a few hundreds of keV higher for UNEDF1 EDF compared to those of SkM* EDF. In Fig. 6, we plot our FAM-RPA results too. The strength functions are almost identical up to the first peak, after which the FAM-RPA calculations show more fragmented second peak or sub-peaks compared to the TDDFT calculations. This spurious behavior of the HO-basis calculation is similar to the TDDFT calculation without the

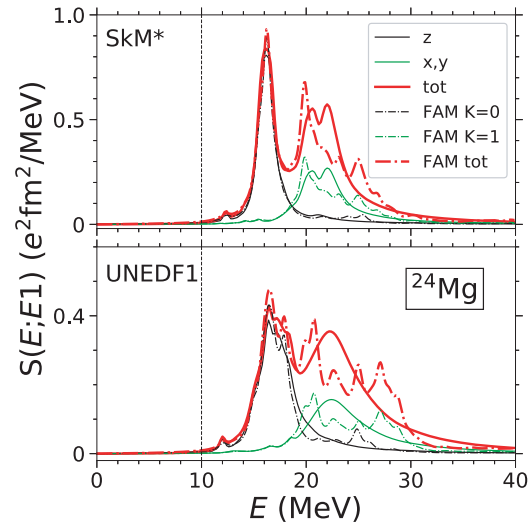

FIG. 6. The calculated strength functions of ^{24}Mg using SkM* and UNEDF1 EDFs, with the TDDFT and the FAM-RPA methods.

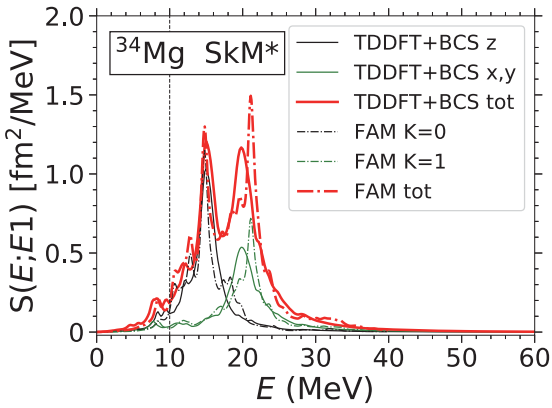

FIG. 7. The calculated strength functions of ^{34}Mg with SkM* EDF using the TDDFT + BCS and the FAM-QRPA methods.

ABC. Both results indicate that the proper treatment of the boundary condition is important to accurately describe the higher excitation energy region of the strength distribution.

For the strength function of ^{24}Mg calculated with SkM* EDF, there are a few calculations using different models. For example, in Ref. [53], the photoabsorption cross section for ^{24}Mg has been calculated with the FAM-RPA method. In Ref. [16] a canonical-basis TDHFB calculation is performed to calculate the $E1$ strength in ^{24}Mg. In particular, the result is consistent with their QRPA results [16]. In Ref. [63], the QRPA calculations using (transformed) HO basis has been performed for the $E1$ strengths in Mg isotopes.

Comparing these three existing results [Fig. 8(g) of Ref. [53], Fig. 2 of Ref. [16], and Fig. 15 of Ref. [63]] with that in the current work which is shown in Fig. 6, it can be summarized that, for all the calculated results, there are unambiguously two peaks at $E \approx 16$ and 22 MeV. The structure or sub-peaks appearing between these two are susceptible to, presumably, either the box size, or the truncation in the single-particle levels, and HO shells used in the respective models. It is rewarding to see such a consistency among independent methods and implementations.

Figure 7 shows the calculated $E1$ strengths for ^{34}Mg using both the TDDFT + BCS and the FAM-QRPA calculations. For the TDDFT + BCS calculations, pairing exists only for neutrons. The pairing strength for neutrons is $V_n = -500$ MeV fm^3. There are 44 single-neutron levels included in the BCS problem. The highest-energy single-particle level has $\epsilon = 3.85$ MeV. To make the two methods comparable, we have fine tuned the pairing strengths in the HFBTHO calculation in such a way that both codes give similar pairing energies in the static calculations.

We see from Fig. 7 that both calculations yield two peaks at $E \approx 15$ and 20 MeV. Again, the second peak from the FAM-QRPA calculation is slightly more fragmented compared to that from the TDDFT+BCS calculations. These results are consistent with the canonical-basis TDHFB results of Ref. [16].

For the neutron-rich oxygen, neon, and magnesium isotopes, the appearance of the $E1$ strength below 10 MeV are of particular interest [16,66,67], as they correspond to the pygmy

TABLE III. The EWSR values of the IVD operator (in e^2 fm^2 MeV) calculated using the current TDDFT code, compared to the ground-state values. For the TDDFT results calculated with Eq. (26), the integrations are taken from 0 to 80 MeV, with $\Gamma = 0$ in Eq. (24).

	TDDFT	g.s. value
^{16}O (SIII-even)	67.1	67.3
^{16}O (SIII-full)	75.0	75.3
^{16}O (SkM*)	72.5	72.8
^{16}O (UNEDF1)	67.0	67.6
^{40}Ca (SkM*)	194.0	194.9
^{40}Ca (UNEDF1)	171.4	172.8
^{24}Mg (SkM*)	113.7	114.3
^{24}Mg (UNEDF1)	101.8	102.9

mode of vibration. It has been shown [16] that the inclusion of the pairing correlation would result in a small enhancement of the fraction of the strengths below 10 MeV, compared to a TDDFT result.

We compute the following PDR fraction [16,17]

$$f_{\rm PDR} = \frac{m_1(E_c)}{m_1} \equiv \frac{\int^{E_c} E \times S(E) dE}{\int E \times S(E) dE}, \tag{32}$$

for the strength functions from TDDFT calculations with and without pairing. The $f_{\rm PDR}$ value for $E_c = 10$ MeV is 2.3% for the $E1$ strength without pairing. When the pairing is included, this quantity increases to 2.7%, which is consistent with the results in Ref. [16].

4. Calculated EWSR

Table III compares the m_1 values calculated with the ground-state expectation value [Eq. (27)], and those calculated with the strength function obtained from the TDDFT method [Eq. (26)]. We see that the m_1 values from the TDDFT and those from Eq. (27) are rather close. The TDDFT values are systematically smaller than those of Eq. (27) by less than 1% of the m_1 values. This indicates the correctness and good precision of the current implementation of the TDDFT code.

The classical TRK sum-rules [Eq. (30)] are 59.2, 148.0, and 88.8 e^2 fm^2 MeV for ^{16}O, ^{40}Ca, and ^{24}Mg, respectively. We have computed the enhancement factor κ using Eq. (31), which are roughly 0.15 and 0.30 for each nucleus using UNEDF1 and SkM* EDFs, respectively.

B. Results for Zr, Mo, and Ru nuclei

In the previous TDDFT + BCS calculations for light spherical and deformed nuclei, we have seen the usefulness of the newly developed code. In this section, we perform systematic calculations for the photoabsorption cross sections of Zr, Mo, and Ru nuclei. For the TDDFT + BCS calculations, the box size is $[-14.5, +14.5]^3$ fm^3, with a uniform grid spacing of 1 fm. In the BCS pairing treatment, 100 and 70 neutron and proton single-particle wave functions are included. The pairing strengths for neutrons and protons are $V_n = -382$ and $V_p = -440$ MeV fm^3, respectively. These are determined to match the pairing energies of ^{106}Mo using the above BCS setup, with those given by the HFB results using the original

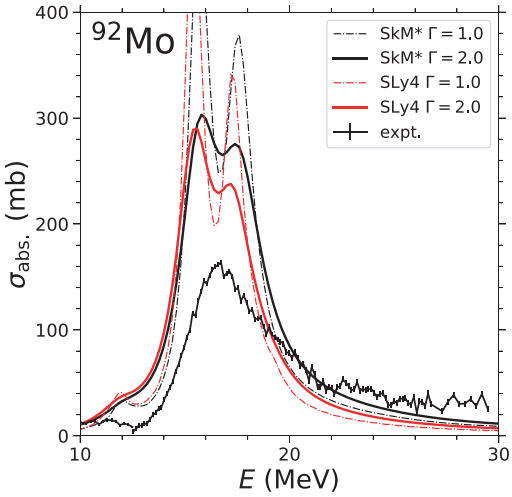

FIG. 8. The IV $E1$ cross sections calculated using the SkM* and SLy4 EDFs with the smoothing parameters $\Gamma = 1.0$ and 2.0 MeV. The experimental data are from Ref. [68], which are extracted from Refs. [69,70].

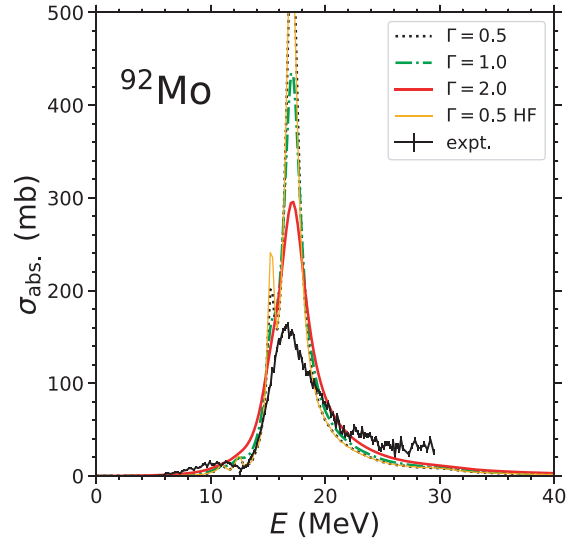

FIG. 9. Similar to Fig. 8, except that the calculations are performed with UNEDF1 EDF for $\Gamma = 0.5$, 1.0, and 2.0 MeV. A photoabsorption cross section calculated without pairing with $\Gamma = 0.5$ MeV is also shown.

UNEDF1 EDF. The ABC has been always included with $\Delta r = 16$ fm and $\eta_0 = 10$ MeV. The above choice of the absorbing parameters seem to be effective for excitation energies larger than 5.5 MeV [9], which is the energy corresponding to the lower end of the GDR peaks.

In this section, we discuss the following related topics: the choice of parameters used to describe the IV $E1$ cross sections of ^{92}Mo (Sec. III B 1); the systematic TDDFT + BCS results for the spherical Zr and Mo nuclei (Sec. III B 2); the calculated potential-energy surfaces for the ground states of neutron-rich Zr, Mo, and Ru isotopes (Sec. III B 3); a case study of ^{100}Mo in terms of the possible shape coexistence (Sec. III B 4); and the systematic predictions of the cross sections for the heavier Zr (Sec. III B 5), Mo, and Ru (Sec. III B 6) isotopes, discussing the dynamical results in connection with the shape coexistence and the evolution of triaxiality with neutron number.

1. The choice of parameters

Figure 8 compares the IV $E1$ cross sections of ^{92}Mo calculated using the SkM* [50] and SLy4 [71] EDFs with the experimental data [68]. The ground state of this semi-magic nucleus ($N = 50$) is calculated to be spherical with various EDFs. For E in the interval of 14 and 20 MeV, we see pronounced strengths for both calculations, as well as experimental data. The calculations with both SkM* and SLy4 show two GDR peaks, which is at variance with the data which appears to have only one peak. The RPA results of ^{92}Mo calculated with SkM* in Ref. [32] shows two peaks between 14 and 20 MeV, which is in agreement of the current results. In Ref. [32] the second peak has a larger strength, whereas in the current work the first one has a larger strength. Similar peak structures are also seen in Ref. [53] for ^{90}Zr, calculated with SkM* EDF.

Figure 9 shows the calculated IV $E1$ cross sections of ^{92}Mo using UNEDF1 EDF for $\Gamma = 0.5$, 1.0, and 2.0 MeV. We see that, as expected, the centroids of the GDR peaks are the same. The photoabsorption cross section calculated with smaller Γ value is more concentrated around the peak with a narrower energy width. Comparing the calculated results with the cross-section data for the $(\gamma,n)+(\gamma,2n)+(\gamma,3n)$ reactions [68], we see that the photoabsorption cross section calculated with $\Gamma = 2.0$ MeV is stilll more concentrated around the peak energy.

Although for ^{92}Mo the calculated results with $\Gamma = 2.0$ MeV overestimate the photoabsorption cross section, for the Zr isotopes, the calculated heights of the GDR peaks are consistent with data using UNEDF1 EDF, as we will see later in Sec. III B 2. Hence, we choose to use $\Gamma = 2.0$ MeV for the remaining calculations in this section. This choice of Γ value is also consistent with the RPA calculations [32], where a 2.0 MeV smoothing parameter was seen to produce reasonable descriptions for these cross-section data.

As shown in Fig. 9, with $\Gamma = 2.0$ MeV, the GDR curve reproduces the rising part of the experimental data. It peaks at $E \approx 17.2$ MeV and reproduces the experimental data of 17.13 MeV. For the lower part of the spectrum, the calculation with $\Gamma = 2.0$ MeV underestimates the experimental cross section. For the result of $\Gamma = 0.5$ MeV, the photoaborption cross section calculated without the proton pairing is also plotted (the neutron pairing vanishes for this nucleus). We see the photoabsorption cross sections calculated with and without the proton pairing are almost identical except for the peaks where those of the unpaired result are slightly higher. When a larger Γ is used, the results with and without the pairing interaction are even closer. Although the inclusion of the pairing seems to have little influence on the IVD vibration calculations, for deformed nuclei, it impacts the shapes of GDR peaks through changing the deformations of the ground states.

2. Results for spherical Zr and Mo isotopes

In this section, we extend the calculation setup described in Sec. III B 1 to calculate the remaining spherical Zr and Mo nuclei where experimental data exist: ^{90,94}Zr and ^{92,94,96,98}Mo.

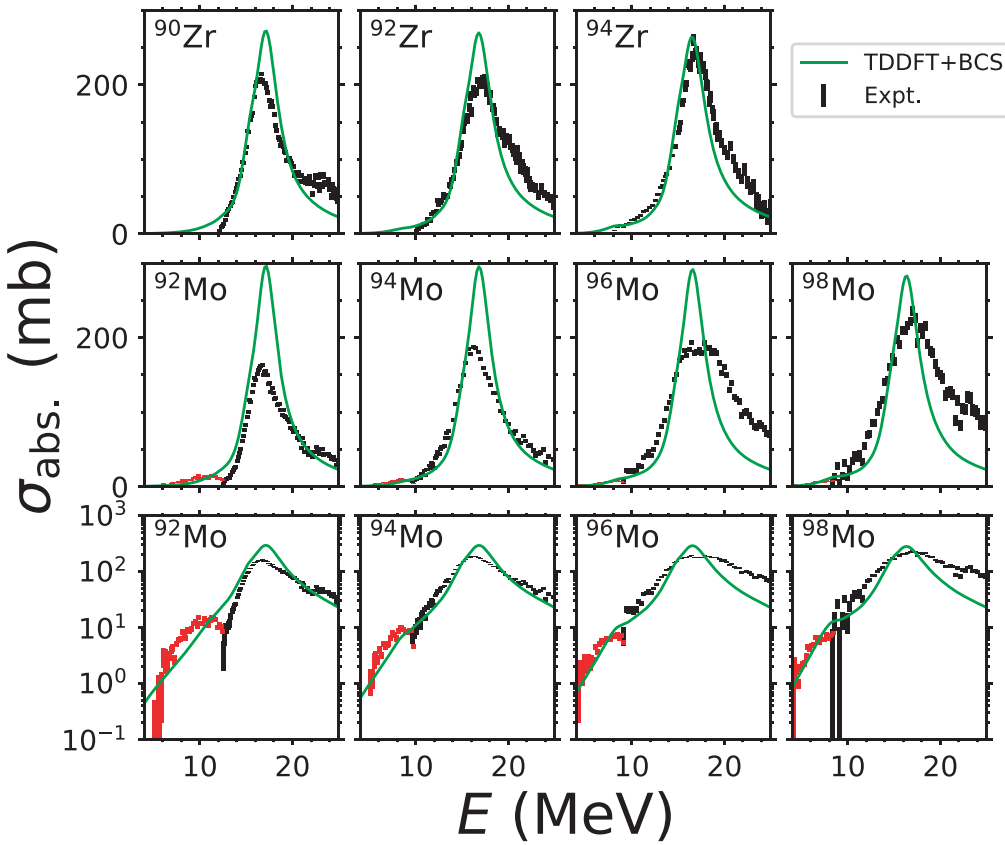

FIG. 10. Calculated photoabsorption cross sections using UNEDF1 EDF, with smoothing parameter $\Gamma = 2.0$ MeV. The experimental data for GDR (red and black crosses) are from Refs. [68,72]. In the third row, the same cross sections for Mo isotopes are plotted in the logarithmic scale. The data for the lower-energy parts (red crosses) are from Refs. [73–77]. The numbers are extracted from Refs. [69,70].

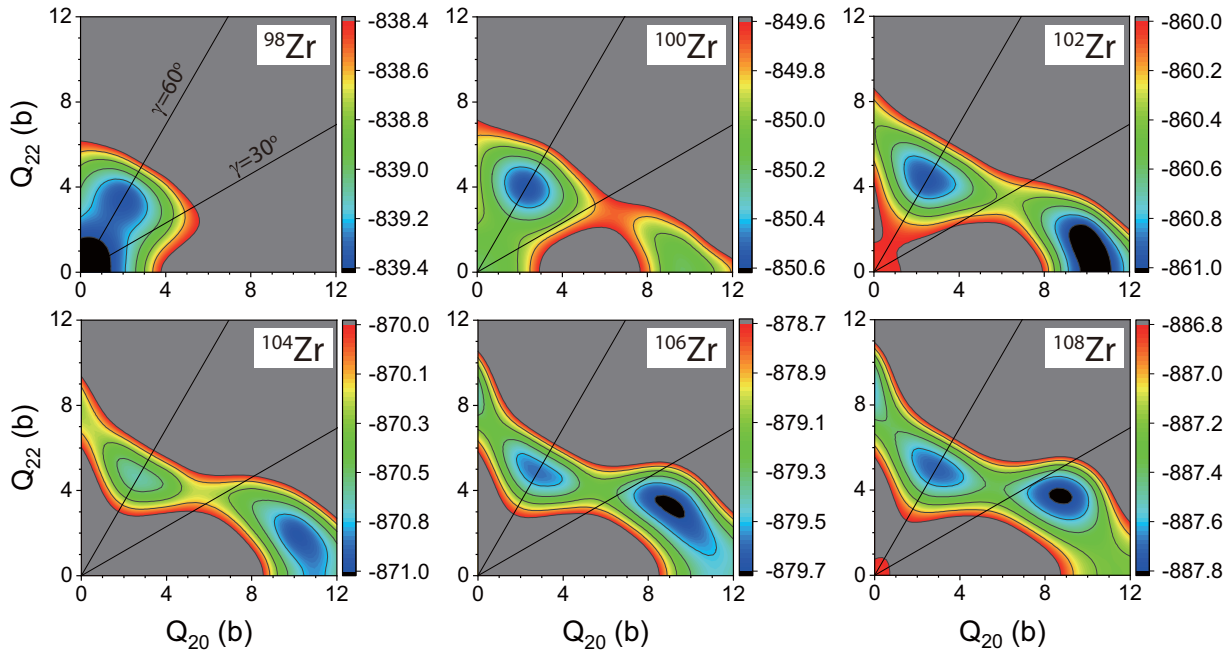

FIG. 11. Calculated potential-energy surfaces for $^{98-108}$Zr, using the UNEDF1 EDF. The energies are in MeV.

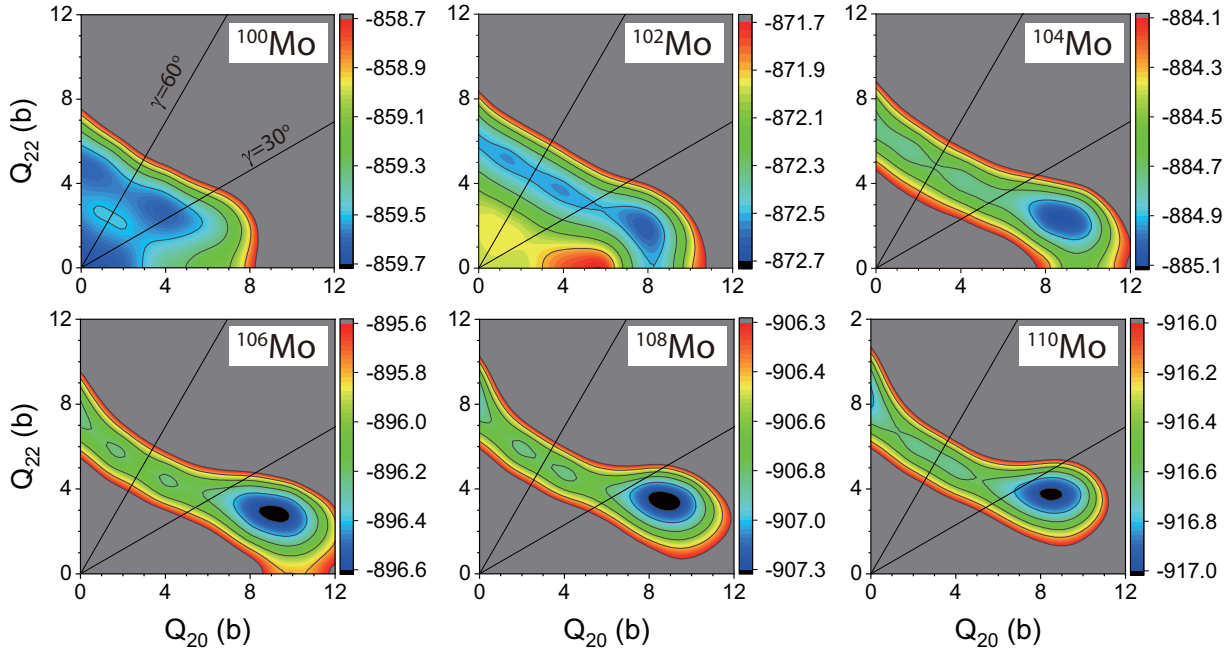

FIG. 12. The same as described in the caption of Fig. 11, except for $^{100-110}$Mo.

The results are shown in Fig. 10. We see that the widths and the centroids of the GDR peaks for ^{90,92,94}Zr are well reproduced by the current calculations. For ^{90,92}Zr, the heights of the GDR peaks are overestimated. For ^{92,94}Mo, the centroids are slightly overestimated. The heights of the GDR peaks of ^{92,94,96}Mo are again overestimated. For ^{96,98}Mo, we see a flattening of the peaks in the experimental data, this might indicate the triaxial deformations of the ground states, as will be discussed in the case of ^{100}Mo in Sec. III B 4.

For the Mo isotopes, the low-energy part ($E \leqslant 10$ MeV) of the cross sections were observed using bremsstrahlung method [73,74,76]. Our calculated results reproduce the existence of the shoulders near $E = 10$ MeV. For the low-energy part ($E < 10$ MeV), the calculated results underestimate the cross-section data in ^{92,94}Mo, and show reasonable agreement with experimental data for ^{96,98}Mo, as well as ^{100}Mo, the latter of which will be discussed in detail in Sec. III B 4.

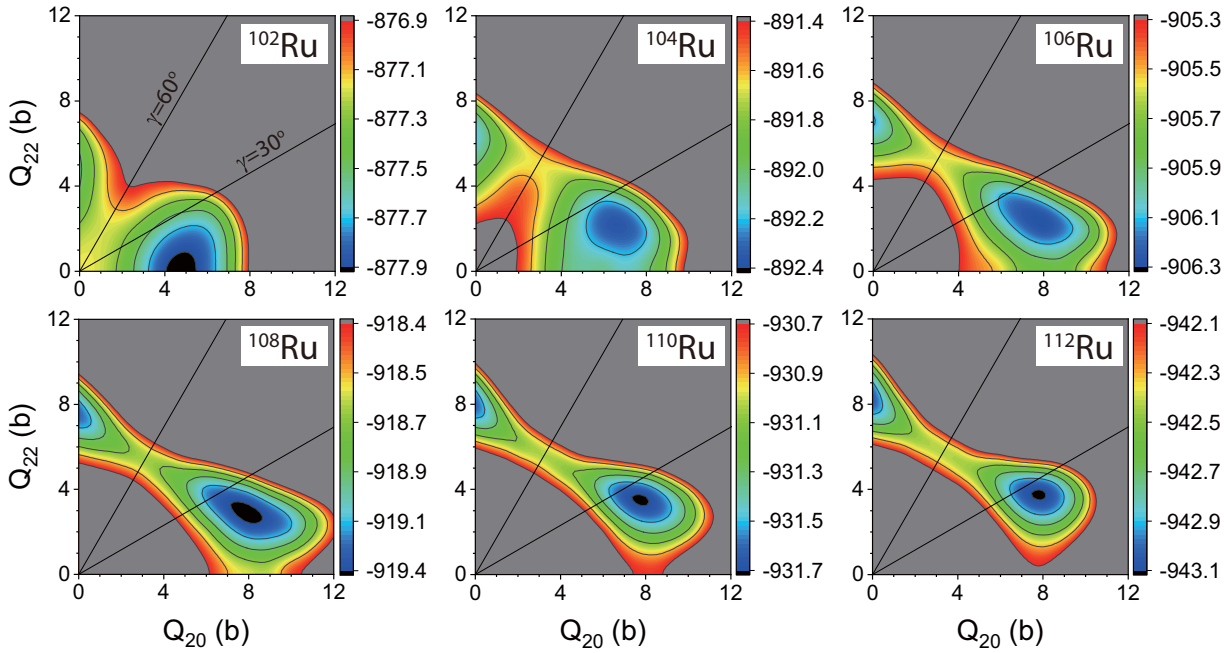

FIG. 13. The same as described in the caption of Fig. 11, except for $^{102-112}$Ru.

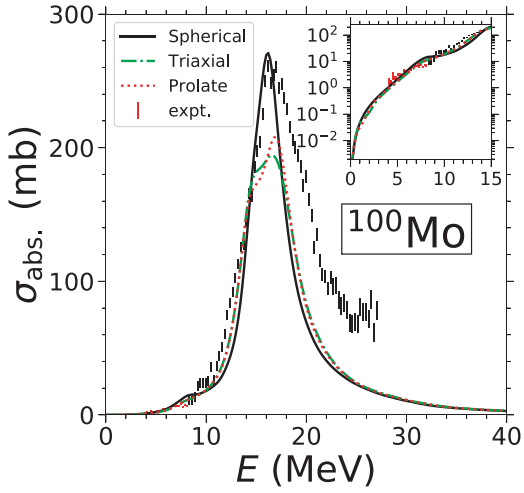

FIG. 14. The cross sections of ^{100}Mo calculated with UNEDF1 EDF, $\Gamma = 2.0$ MeV. The black solid line corresponds to the spherical ground state as shown in Fig. 12. The green dashed line corresponds to the triaxial minimum in the energy surface of ^{100}Mo, with $(Q_{20}, Q_{22}) = (3.5, 2.4)$ b. The above two curves are based on results without constraints on the quadrupole moments. The red dotted line corresponds to a prolate deformation which has been constrained to have $Q_{20} = 5.0$ b. The experimental data are extracted from Refs. [69,70].

3. Static potential energy surfaces for neutron-rich Zr, Mo, and Ru isotopes

Before showing the calculated IV $E1$ photoabsorption cross section of these neutron-rich nuclei, it is necessary to have some idea about the potential-energy surfaces of quadrupole deformations. Figures 11–13 display the potential-energy surfaces for even-even $^{98-108}$Zr, $^{100-110}$Mo, and $^{102-112}$Ru nuclei, calculated with UNEDF1 EDF. The constrained HFB calculations for these potential-energy surfaces are performed with the HFODD code (version 2.68h [28]). For these HFB+LN calculations, there are 1140 ($N = 17$) spherical HO bases included; the original pairing strengths and energy cutoff on the quasiparticle spectra are used [51].

For the Zr isotopes, the ground states for $50 \leqslant N \leqslant 58$ are spherical due to their closeness to the $Z = 40$ subshell closure. For ^{100,102}Zr ($N = 60, 62$), the ground states show the coexistence of prolate and oblate minima, with the prolate minimum being slightly lower energetically in ^{102}Zr. For Zr isotopes with $N \geqslant 64$, the prolate minima move to a static triaxial deformation, with the oblate minima staying slightly higher in energy.

The evolution of the minima of the neutron-rich Mo and Ru isotopes can be seen in Figs. 12 and 13. In general, we observe a triaxial minimum near prolately deformed region which is developed in the $N = 60$ isotopes (^{102}Mo and ^{104}Ru). This minimum increases γ with increasing neutron number. For all the isotopes with $58 \leqslant N \leqslant 70$, the current results predict a finite γ deformation.

The shape evolution and shape coexistence near the ground states of the neutron-rich zirconium isotopes are particularly interesting. With recent advances in the rare isotope facilities, the experimental low-energy spectra for the most neutron-rich isotopes in the Zr, Mo, and Ru nuclei [78–80] are becoming more and more available. If we examine the experimental and theoretical literatures, then it is fair to say that the current static calculations are in reasonable agreement with the experimental data. The potential-energy surfaces obtained using UNEDF parameters [81] are somewhat more rigid in the γ deformation compared with theoretical calculations using other models and parameters [82–88]. Thus, we continue our dynamic survey using UNEDF1 EDF. The main conclusions about the variations of GDR peaks due to quadrupole deformation obtained here can be expanded to other parameters or even other mean-field models.

4. A case study: ^{100}Mo

In Sec. III A 2 we have shown that the current TDDFT + BCS calculations give good description for the GDR peaks and the lower part of the strengths for the spherical nuclei in this mass region. This section discusses the influence of the deformation on the GDR peak of ^{100}Mo.

In Fig. 14 we show the calculated results of ^{100}Mo using the UNEDF1 EDF and $\Gamma = 2.0$ MeV. The potential-energy surface of ^{100}Mo show significant softness around the spherical minimum, with a triaxial minimum being very low in energy; see Fig. 12. Hence, the cross-section curves based on both minima are calculated and plotted in Fig. 14. In addition, a red dotted curve is included with the quadrupole moments being artificially constrained to be $(Q_{20}, Q_{22}) = (5.0, 0.0)$ b.

In Fig. 14, we see that the calculated height of the GDR peak for the spherical minimum reproduces that of the experimental data. The width has been underestimated. The TRK sum rule value is 361.8 e^2 fm^2 MeV for this nucleus. The EWSR from the TDDFT + BCS result is 415 e^2 fm^2 MeV ($\kappa = 0.15$). The shape of the GDR peak based on the prolate deformation is similar to that based on the triaxial deformation, except that the peak at the higher energy is more pronounced. The relative heights of the peaks are related to the deformation they are based on, as will be discussed in Sec. III B 5. The cross sections calculated based on the three minima well reproduce the low-energy ($E < 10$ MeV) part of the experimental data. Comparing our calculated GDR peaks based on spherical, prolate, and triaxial minima with that of the experimental data, it seems that the data support an explanation that the IVD vibration is based on a spherical minimum.

5. Dynamical results for Zr isotopes: Shape coexistence

The systematic calculations of TDDFT+BCS for Zr, Mo, and Ru isotopes are displayed in Figs. 15 and 17. The relevant information on the static results before the time propagation is listed in Table IV. These HF+BCS calculations using the finite-difference method are without deformation constraints.

For the triaxially deformed minima in $^{104-108}$Zr, $^{102-110}$Mo, and $^{104-112}$Ru, the HF+BCS calculations give smaller γ compared to that of the HFB+LN results using HFODD (Figs. 11–13). Specifically, for the softest nucleus, the triaxially deformed ^{110}Mo, the HFB+LN calculation using HFODD gives quadrupole

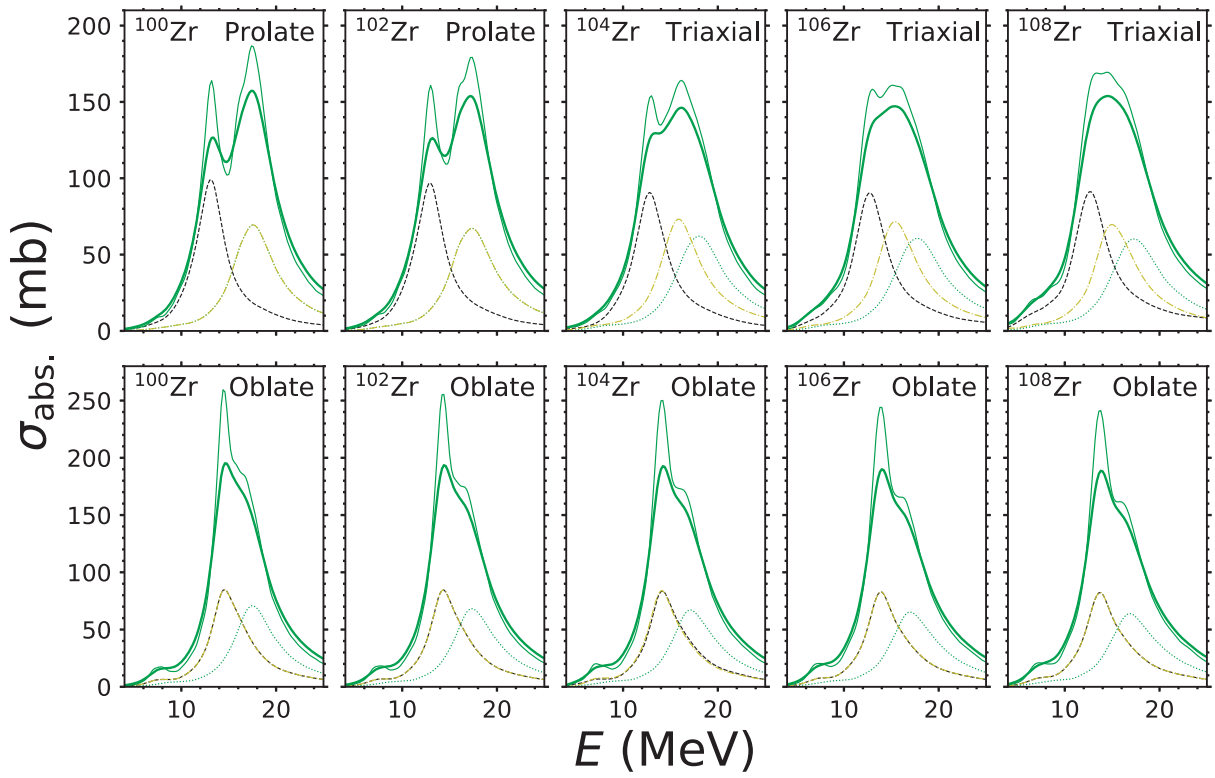

FIG. 15. Photoabsorption cross sections calculated for $^{100-108}$Zr with UNEDF1 EDF with smoothing parameter $\Gamma = 2.0$ MeV (thick line) and 1.0 MeV (thin line). The plots in upper row correspond to the results based on the prolate minima for ^{100,102}Zr, and the triaxial minima for $^{104-108}$Zr; the plots in the lower row correspond to those based on the oblate minima, see Fig. 11. The thinner green lines indicate results with $\Gamma = 1.0$ MeV.

moments $(Q_{20}^{\mathrm{HFB+LN}}, Q_{22}^{\mathrm{HFB+LN}}) \approx (8.5, 3.5)$ b (see Fig. 12). Without pairing, the HFODD calculation gives $(Q_{20}^{\mathrm{HF}}, Q_{22}^{\mathrm{HF}}) \approx (9.4, 4.0)$ b. Before performing dynamic calculation, the static HF+BCS calculation in the Cartesian coordinate space gives $(Q_{20}, Q_{22}) \approx (9.2, 3.9)$ b.

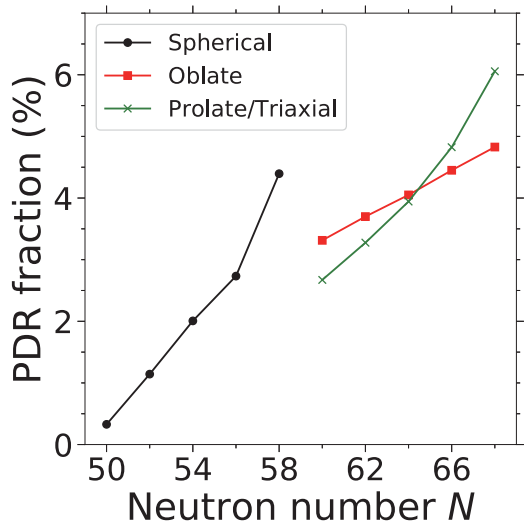

FIG. 16. The fraction of the strengths for IVD resonances below $E_c = 10$ MeV [Eq. (32)] for zirconium isotopes with spherical, prolate(for ^{100,102}Zr)/triaxial(for ^{104,106,108}Zr), and oblate deformations. The smoothing parameter $\Gamma = 0.5$ MeV is used in the calculation. The integrations for the total strengths are taken from 0 to 80 MeV.

For ^{100,102}Zr shown in Fig. 15 the GDR peaks split into two, with the sub-peak at a slightly lower energy ($E \approx 13$ MeV) and the height of the peak is lower than that at the higher energy ($E \approx 18$ MeV). For ^{104}Zr, the IVD vibrations are based on a weakly triaxial minimum, see Fig. 15. The peaks at the higher excitation energies become broader. For ^{106,108}Zr, the two peaks merge to form one broader peak.

The features of the GDR peaks can be understood qualitatively. For a spherical nucleus, the GDR peaks corresponding to the three vibrational modes are identical due to the spherical symmetry. When the nucleus acquires an axially symmetric deformation, the GDR peaks split into two groups: (1) a mode corresponding to a vibration along the symmetry axis ($K = 0$ mode); and (2) two modes corresponding to the vibrations along the axes perpendicular to the symmetry axis ($K = \pm 1$ modes). For a prolate shape, intuitively, because of the larger material extension, the potential is enlongated along the symmetry axis. Hence, the energy cost is lower for the $K = 0$ mode, compared to the $K = \pm 1$ modes. While the peak for the $K = 0$ mode shifts to a lower energy, the contribution of this mode to the total strength becomes larger than those of the $K = \pm 1$ modes. Similar effects can be found from light to heavy spherical nuclei, where the total GDR peak shifts to a lower energy and the strength becomes larger and/or broader.

For these neutron-rich Zr isotopes, the oblate minima appear at relatively low energies. As discussed above, the peaks

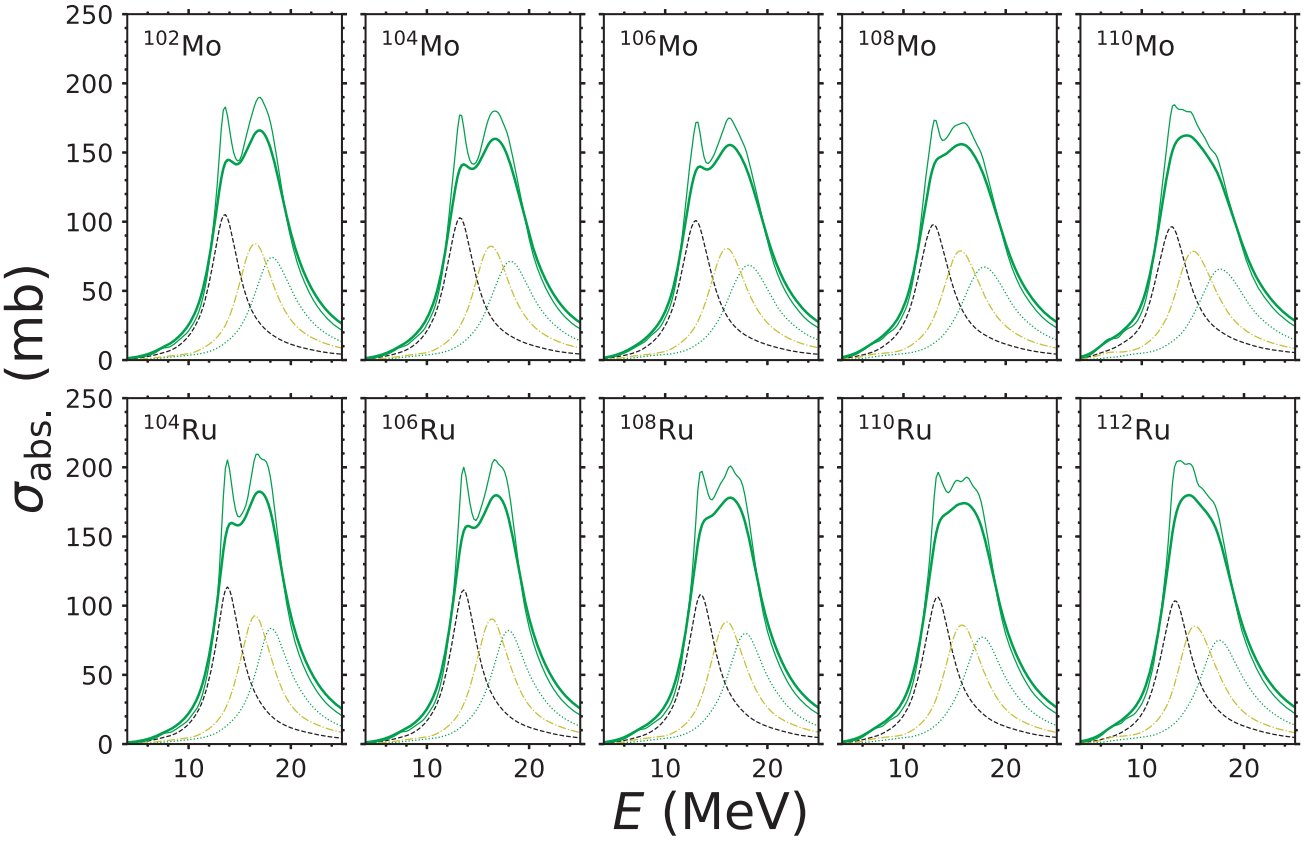

FIG. 17. The same as described in the caption of Fig. 15, except for $^{102-110}$Mo and $^{104-112}$Ru.

corresponding to the two longer axes ($K = \pm 1$) appear at lower energies, and the strengths are larger compared to that from the shorter axis ($K = 0$). This results in the peaks of the total cross section at the lower energies ($E \approx 14$ MeV) considerably higher than those at higher energies ($E \approx 18$ MeV) and higher than those of the prolate deformation. Because of the large smoothing parameter ($\Gamma = 2.0$ MeV), the second peaks appear to be shoulders of the first higher peaks for these nuclei.

Figure 16 plots the PDR fraction $f_{\rm PDR}$ below $E_c = 10$ MeV for Zr isotopes based on different deformations. With the same deformation, the $f_{\rm PDR}$ values increase with neutron excess. From spherical to deformed nuclei, we see a small decrease of the $f_{\rm PDR}$ value at $N = 60$, which agrees with the previous studies [17,29]. For the case of the transition from a spherical to a prolate deformation, this is a net result of (1) the decrease of energy of the $K = 0$ mode, and the increase of the energy of the $K = \pm 1$ modes, as well as (2) an enhanced contribution in the total strength from the $K = 0$ mode, as pointed out in Ref. [89]. For the transition from a spherical to an oblate deformation, similar effects are also responsible for the decrease of the PDR fraction. For the oblate deformation, there is a plateau structure below $E = 10$ MeV, which is the main contribution to the $f_{\rm PDR}$ value. The slope of $f_{\rm PDR}$ curve are smaller for the oblate deformation compared to that of the prolate deformation. This is because the oblate deformations are relatively constant, whereas the prolate minima become weak triaxial with increasing neutron number.

6. Dynamical results for Mo and Ru isotopes: Triaxial deformation

Figure 17 plots the IVD cross sections calculated for the Mo and Ru isotopes with $60 \leqslant N \leqslant 68$. In the current work, these nuclei are calculated to be triaxial. The properties concerning the ground states are listed in Table IV. For $^{102-106}$Mo, the GDR peaks appear to include two sub-peaks instead of three, due to the weak γ deformation and large Γ. For ^{110}Mo, the three peaks due to the vibrations in the three Cartesian directions merge into one broad peak. It is interesting to note that from ^{100}Mo to ^{102}Mo one sees a transition in deformation from soft spherical to a soft triaxial shape; see Fig. 12. The total cross section for ^{100}Mo has been discussed in Sec. III B 4.

For deformed nuclei, the experimental data seem to indicate a smaller smoothing parameter compared to that of the spherical ones [65]. Thus, in Figs. 15 and 17, we plot the same total cross sections with a smaller $\Gamma = 1.0$ MeV. We can see that, as expected, the heights of the GDR peaks are larger compared to those with $\Gamma = 2.0$ MeV. With better resolution, we can see more detailed structures due to the different subpeaks.

Figure 18(a) plots the energy differences corresponding to the three GDR peaks due to the K modes along the three axes. The $Q_2 \equiv \sqrt{Q_{20}^2 + Q_{22}^2}$ is constrained to be 10.4 b while

TABLE IV. The ground-state (and the coexisting minima for Zr isotopes) properties, the pairing energies, the quadrupole moment, and the triaxial parameter (γ) of $^{100-108}$Zr, $^{102-110}$Mo, and $^{104-112}$Ru calculated with the HF+BCS code with the finite-difference method. The Q_{22} value is connected with the Q_{20} and γ values through $Q_{22} = Q_{20} \tan\gamma$. The pairing strengths for neutrons and protons are -382 and -440 MeV fm^3, respectively.

Nuclei	$E^{\rm n}_{\rm pair}$ (MeV)	$E^{\rm p}_{\rm pair}$ (MeV)	Q_{20} (b)	γ (deg)	$m_1^{\rm TDDFT}$ (e^2 fm^2 MeV)	$m_1^{\rm g.s.}$ (e^2 fm^2 MeV)
^{100}Zr	−4.842	−3.778	2.286	60	410.3	420.7
	−2.676	−3.488	9.894	0	410.4	421.0
^{102}Zr	−7.846	−3.541	2.591	60	415.1	426.0
	−3.775	−3.435	10.282	0	416.3	426.4
^{104}Zr	−2.223	−2.711	9.555	16	411.9	431.6
	−3.854	−3.173	2.502	60	423.8	431.1
^{106}Zr	−1.717	−2.457	9.352	19	439.2	436.6
	−2.543	−3.132	2.943	60	426.8	436.1
^{108}Zr	−0.670	−2.450	9.102	19	444.9	441.3
	−1.165	−3.024	3.161	60	429.8	441.0
^{102}Mo	−4.686	−3.362	8.454	15	422.9	433.6
^{104}Mo	−4.178	−2.984	9.100	16	428.6	439.5
^{106}Mo	−3.865	−2.624	10.010	16	433.4	445.0
^{108}Mo	−4.240	−2.369	9.759	18	437.9	450.2
^{110}Mo	−4.007	−2.322	9.200	23	453.0	455.3
^{104}Ru	−5.192	−2.894	7.871	16	433.9	445.8
^{106}Ru	−5.473	−2.777	8.110	16	438.2	452.0
^{108}Ru	−5.953	−2.271	7.957	18	447.7	457.9
^{110}Ru	−5.363	−2.116	8.442	19	450.7	463.6
^{112}Ru	−5.113	−1.716	8.160	24	455.7	468.9

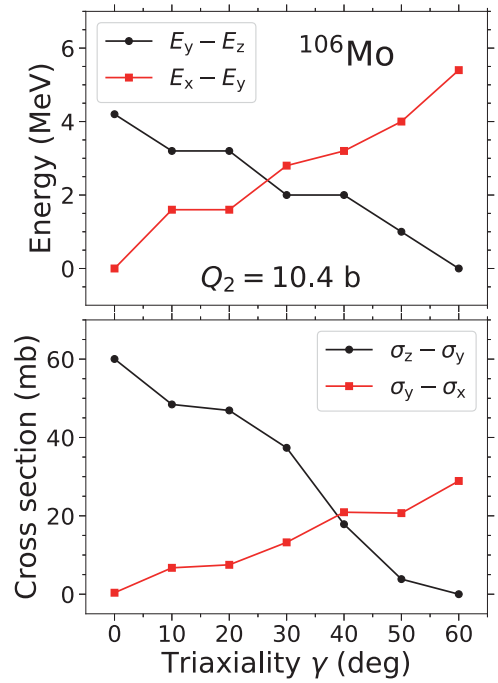

FIG. 18. The upper panel are the energy differences of peaks corresponding to the vibrations along the $y-$ and $z-$ axis ($E_y - E_z$), as well as along the $x-$ and $y-$ axis for $\gamma = 0^\circ - 60^\circ$ of ^{106}Mo. The lower panel are the calculated relative cross sections corresponding to the energies in the upper panel, that is, $\sigma_{\rm x,y,z} \equiv \sigma_{\rm abs.}(E_{\rm x,y,z})$.

γ deformation is constrained to vary from 0° to 60°. It can be seen that the energy difference between E_y and E_z, which corresponds to the vibration along the long and medium axes, respectively, decreases monotonically as γ increases from a prolate to an oblate deformation. Whereas the energy difference between E_x and E_y increases with γ deformation. For axial deformations, the energy split of the two peaks are larger for the oblate deformation than that of the prolate deformation.

Figure 18(b) shows the relative heights of the GDR cross sections corresponding to the vibration modes along the three axes as a function of the triaxial deformation. We see that the height corresponding to the vibration of the long axis (z axis) is always larger than that of the medium axis (y axis). Similarly, $\sigma_{\rm abs.}(E_{\rm y})$ is always larger than $\sigma_{\rm abs.}(E_{\rm x})$. This can be qualitatively explained: the further the material extends the lower the peak energy becomes; the lower the energy becomes, the larger the height becomes. With increasing γ, $\sigma_{\rm abs.}(E_{\rm z}) - \sigma_{\rm abs.}(E_{\rm y})$ decreases continuously until $\sigma_{\rm abs.}(E_{\rm z}) = \sigma_{\rm abs.}(E_{\rm y})$ for an oblate deformation.

We end this section by emphasizing the interests associated with the current study. The experimental signature of the triaxial deformation in the nuclear ground state is not well established, which is mainly due to the theoretical challenges in uniquely connecting the spectroscopic observables with the triaxial degree of freedom. The investigations presented in this section may provide prospects to establish a firm connection between the photoabsorption cross section data and the ground-state triaxial deformation. Indeed, for the heavier Mo and Ru isotopes, if future experiments allow for resolving the general shapes (peak heights and splittings) of the individual peaks originated from different K modes, then it is possible to determine the triaxiality parameter of the ground state by comparing the experimental plot similar to Fig. 18.

IV. SUMMARY

Based on a previous computer code developed for the nuclear density-functional theory (DFT), we present a further development, enabling the time-dependent DFT (TDDFT) calculations with BCS pairing. We benchmark the code by comparing its calculated response functions of the dipole moment of ^{16}O with that of an existing 3D TDDFT code, Sky3D. Although the response functions for ^{16}O are sensitive to a few subtle factors (time-odd mean fields, treatment of boundary conditions, etc.), a remarkable agreement has been found between the two codes, as long as those factors are carefully considered.

To apply the TDDFT + BCS in its linearized limit and describe the isovector (IV) electric dipole ($E1$) observables, we carry out finite-amplitude method for quasiparticle random-phase approximation (FAM-QRPA) for a few light spherical

(^{16}O, ^{40}Ca) and axially deformed (^{24,34}Mg) nuclei, and compare the calculated IV $E1$ properties with those resulted from the TDDFT + BCS calculations. The comparisons are acceptable up to the first peak at $E \approx 20$ MeV. Beyond that, the FAM-QRPA calculations based on the harmonic-oscillator basis give more fragmented peaks compared to that of the TDDFT + BCS calculations employing the absorbing boundary condition.

Using the UNEDF1 energy-density functional (EDF), the current TDDFT + BCS calculations provide reasonable descriptions for both the giant dipole resonance and the low-energy part of the IV $E1$ photoabsorption cross section for spherical Zr and Mo isotopes, where experimental data exist.

For heavier Zr isotopes, the calculated potential-energy surfaces show coexisting minima. The predicted $E1$ photoabsorption cross sections reflect typical features depending on the local minima that they are based upon.

For heavier Mo and Ru isotopes, the ground states are predicted to be triaxial. The predicted cross sections show features that distinguish them from the spherical ones. For Mo isotopes considered here, the predicted onset of the triaxial deformation which occurs in ^{102}Mo ($N = 60$), is only two neutrons larger than the isotope, ^{100}Mo, in which experimental data exist. The systematic measurements of the photonuclear experiments on these Mo isotopes are desired for further analysis of the ground-state triaxial deformation.

ACKNOWLEDGMENTS

Useful discussions with T. Nakatsukasa, W. Nazarewicz, and P. Stevenson are gratefully acknowledged. The current work is supported by National Natural Science Foundation of China (Grants No. 11705038 and No. 12075068), JSPS KAKENHI Grants No. 16K17680 and No. 20K03964, the JSPS-NSFC Bilateral Program for the Joint Research Project on "Nuclear mass and life for unravelling mysteries of r-process," and the Deutsche Forschungsgemeinschaft (DFG, German Research Foundation)—Projektnummer 279384907—SFB 1245. Y.S. thanks the HPC Studio at Physics Department of Harbin Institute of Technology for computing resources allocated through INSPUR-HPC@PHY.HIT. A part of the numerical calculations were performed at the Oakforest-PACS Systems through the Multidisciplinary Cooperative Research Program of the Center for Computational Sciences, University of Tsukuba.

[1] Y. Engel, D. Brink, K. Goeke, S. Krieger, and D. Vautherin, Nucl. Phys. A **249**, 215 (1975).
[2] P. Bonche, S. E. Koonin, and J. W. Negele, Phys. Rev. C **13**, 1226 (1976).
[3] R. Y. Cusson, R. K. Smith, and J. A. Maruhn, Phys. Rev. Lett. **36**, 1166 (1976).
[4] J. W. Negele, Rev. Mod. Phys. **54**, 913 (1982).
[5] T. Nakatsukasa, K. Matsuyanagi, M. Matsuo, and K. Yabana, Rev. Mod. Phys. **88**, 045004 (2016).
[6] A. S. Umar, V. E. Oberacker, and C. Simenel, Phys. Rev. C **92**, 024621 (2015).
[7] C. Simenel, Eur. Phys. J. A **48**, 152 (2012).
[8] S. Burrello, M. Colonna, G. Colò, D. Lacroix, X. Roca-Maza, G. Scamps, and H. Zheng, Phys. Rev. C **99**, 054314 (2019).
[9] T. Nakatsukasa and K. Yabana, Phys. Rev. C **71**, 024301 (2005).
[10] J. A. Maruhn, P. G. Reinhard, P. D. Stevenson, J. R. Stone, and M. R. Strayer, Phys. Rev. C **71**, 064328 (2005).
[11] A. S. Umar and V. E. Oberacker, Phys. Rev. C **73**, 054607 (2006).
[12] G. Scamps and C. Simenel, Nature **564**, 382 (2018).
[13] I. Stetcu, A. Bulgac, P. Magierski, and K. J. Roche, Phys. Rev. C **84**, 051309(R) (2011).
[14] A. Bulgac, P. Magierski, K. J. Roche, and I. Stetcu, Phys. Rev. Lett. **116**, 122504 (2016).
[15] P. Magierski, K. Sekizawa, and G. Wlazłowski, Phys. Rev. Lett. **119**, 042501 (2017).
[16] S. Ebata, T. Nakatsukasa, T. Inakura, K. Yoshida, Y. Hashimoto, and K. Yabana, Phys. Rev. C **82**, 034306 (2010).
[17] S. Ebata, T. Nakatsukasa, and T. Inakura, Phys. Rev. C **90**, 024303 (2014).
[18] Y. Hashimoto, Eur. Phys. J. A **48**, 55 (2012).
[19] Y. Hashimoto, Phys. Rev. C **88**, 034307 (2013).
[20] Y. Hashimoto and G. Scamps, Phys. Rev. C **94**, 014610 (2016).
[21] G. Scamps and Y. Hashimoto, Phys. Rev. C **96**, 031602(R) (2017).
[22] K. Washiyama and T. Nakatsukasa, Phys. Rev. C **96**, 041304(R) (2017).
[23] Y. Shi, Phys. Rev. C **98**, 014329 (2018).
[24] J. Maruhn, P.-G. Reinhard, P. Stevenson, and A. Umar, Comput. Phys. Commun. **185**, 2195 (2014).
[25] B. Schuetrumpf, P. G. Reinhard, P. D. Stevenson, A. S. Umar, and J. A. Maruhn, Comput. Phys. Commun. **229**, 211 (2018).
[26] J. Dobaczewski and J. Dudek, Comput. Phys. Commun. **102**, 166 (1997).
[27] J. Dobaczewski, W. Satuła, B. Carlsson, J. Engel, P. Olbratowski, P. Powałowski, M. Sadziak, J. Sarich, N. Schunck, A. Staszczak, M. Stoitsov, M. Zalewski, and H. Zduńczuk, Comput. Phys. Commun. **180**, 2361 (2009).
[28] N. Schunck, J. Dobaczewski, W. Satuła, P. Baczyk, J. Dudek, Y. Gao, M. Konieczka, K. Sato, Y. Shi, X. Wang, and T. Werner, Comput. Phys. Commun. **216**, 145 (2017).
[29] T. Inakura, T. Nakatsukasa, and K. Yabana, Phys. Rev. C **84**, 021302(R) (2011).
[30] G. Scamps and D. Lacroix, Phys. Rev. C **88**, 044310 (2013).
[31] G. Scamps and D. Lacroix, Phys. Rev. C **89**, 034314 (2014).
[32] J. Kvasil, P. Vesely, V. O. Nesterenko, W. Kleinig, P.-G. Reinhard, and S. Frauendorf, Int. J. Mod. Phys. E **18**, 975 (2009).
[33] J. Bardeen, L. N. Cooper, and J. R. Schrieffer, Phys. Rev. **108**, 1175 (1957).
[34] P. Ring and P. Schuck, *The Nuclear Many-Body Problem* (Springer-Verlag, Berlin, 1980).
[35] M. Bender, K. Rutz, P.-G. Reinhard, and J. Maruhn, Eur. Phys. J. A **8**, 59 (2000).

[36] J. Dobaczewski, H. Flocard, and J. Treiner, Nucl. Phys. A **422**, 103 (1984).

[37] S. Fracasso, E. B. Suckling, and P. D. Stevenson, Phys. Rev. C **86**, 044303 (2012).

[38] L. Guo, C. Simenel, L. Shi, and C. Yu, Phys. Lett. B **782**, 401 (2018).

[39] J. Dobaczewski and J. Dudek, Phys. Rev. C **52**, 1827 (1995).

[40] V. Hellemans, P.-H. Heenen, and M. Bender, Phys. Rev. C **85**, 014326 (2012).

[41] P. D. Stevenson, E. B. Suckling, S. Fracasso, M. C. Barton, and A. S. Umar, Phys. Rev. C **93**, 054617 (2016).

[42] G. Scamps, D. Lacroix, G. F. Bertsch, and K. Washiyama, Phys. Rev. C **85**, 034328 (2012).

[43] B. Schuetrumpf and W. Nazarewicz, Phys. Rev. C **92**, 045806 (2015).

[44] C. Q. He, J. C. Pei, Y. Qiang, and N. Fei, Phys. Rev. C **99**, 054318 (2019).

[45] M. N. Harakeh and A. van der Woude, *Giant Resonances: Fundamental High-Frequency Modes of Nuclear Excitation* (Oxford University Press, London, 2001).

[46] P. Stevenson (private communication).

[47] N. Hinohara, M. Kortelainen, W. Nazarewicz, and E. Olsen, Phys. Rev. C **91**, 044323 (2015).

[48] N. Hinohara, Phys. Rev. C **100**, 024310 (2019).

[49] A. Bohr and B. R. Mottelson, *Nuclear Structure, vol. II* (W. A. Benjamin, Reading, 1975).

[50] J. Bartel, P. Quentin, M. Brack, C. Guet, and H.-B. Håkansson, Nucl. Phys. A **386**, 79 (1982).

[51] M. Kortelainen, J. McDonnell, W. Nazarewicz, P.-G. Reinhard, J. Sarich, N. Schunck, M. V. Stoitsov, and S. M. Wild, Phys. Rev. C **85**, 024304 (2012).

[52] J. Piekarewicz, Phys. Rev. C **73**, 044325 (2006).

[53] T. Inakura, T. Nakatsukasa, and K. Yabana, Phys. Rev. C **80**, 044301 (2009).

[54] Q. Wu, B. S. Hu, F. R. Xu, Y. Z. Ma, S. J. Dai, Z. H. Sun, and G. R. Jansen, Phys. Rev. C **97**, 054306 (2018).

[55] K. Liu and N. V. Giai, Phys. Lett. B **65**, 23 (1976).

[56] T. Nakatsukasa, T. Inakura, and K. Yabana, Phys. Rev. C **76**, 024318 (2007).

[57] P. Avogadro and T. Nakatsukasa, Phys. Rev. C **84**, 014314 (2011).

[58] M. Kortelainen, N. Hinohara, and W. Nazarewicz, Phys. Rev. C **92**, 051302(R) (2015).

[59] M. Stoitsov, J. Dobaczewski, W. Nazarewicz, and P. Ring, Comput. Phys. Commun. **167**, 43 (2005).

[60] M. Stoitsov, N. Schunck, M. Kortelainen, N. Michel, H. Nam, E. Olsen, J. Sarich, and S. Wild, Comput. Phys. Commun. **184**, 1592 (2013).

[61] R. N. Perez, N. Schunck, R.-D. Lasseri, C. Zhang, and J. Sarich, Comput. Phys. Commun. **220**, 363 (2017).

[62] S. Péru and H. Goutte, Phys. Rev. C **77**, 044313 (2008).

[63] C. Losa, A. Pastore, T. Døssing, E. Vigezzi, and R. A. Broglia, Phys. Rev. C **81**, 064307 (2010).

[64] M. Stoitsov, M. Kortelainen, T. Nakatsukasa, C. Losa, and W. Nazarewicz, Phys. Rev. C **84**, 041305(R) (2011).

[65] T. Oishi, M. Kortelainen, and N. Hinohara, Phys. Rev. C **93**, 034329 (2016).

[66] L.-G. Cao and Z.-Y. Ma, Phys. Rev. C **71**, 034305 (2005).

[67] K. Wang, M. Kortelainen, and J. C. Pei, Phys. Rev. C **96**, 031301(R) (2017).

[68] H. Beil, R. Bergère, P. Carlos, A. Leprêtre, A. D. Miniac, and A. Veyssière, Nucl. Phys. A **227**, 427 (1974).

[69] Russia Lomonosov Moscow State University Skobeltsyn Institute of Nuclear Physics Centre for Photonuclear Experiments Data database, Nuclear Reaction Database (EXFOR), http://cdfe.sinp.msu.ru/exfor/index.php.

[70] USA National Nuclear Data Center database CSISRS and EXFOR Nuclear reaction experimental data, http://www.nndc.bnl.gov/exfor/exfor00.htm.

[71] E. Chabanat, P. Bonche, P. Haensel, J. Meyer, and R. Schaeffer, Nucl. Phys. A **635**, 231 (1998).

[72] B. L. Berman, J. T. Caldwell, R. R. Harvey, M. A. Kelly, R. L. Bramblett, and S. C. Fultz, Phys. Rev. **162**, 1098 (1967).

[73] G. Rusev, E. Grosse, M. Erhard, A. Junghans, K. Kosev, K. D. Schilling, R. Schwengner, and A. Wagner, Eur. Phys. J. A **27**, 171 (2006).

[74] G. Rusev, R. Schwengner, F. Dönau, M. Erhard, E. Grosse, A. R. Junghans, K. Kosev, K. D. Schilling, A. Wagner, F. Bečvář, and M. Krtička, Phys. Rev. C **77**, 064321 (2008).

[75] G. Rusev, R. Schwengner, R. Beyer, M. Erhard, E. Grosse, A. R. Junghans, K. Kosev, C. Nair, K. D. Schilling, A. Wagner, F. Dönau, and S. Frauendorf, Phys. Rev. C **79**, 061302(R) (2009).

[76] M. Erhard, A. R. Junghans, C. Nair, R. Schwengner, R. Beyer, J. Klug, K. Kosev, A. Wagner, and E. Grosse, Phys. Rev. C **81**, 034319 (2010).

[77] H. Utsunomiya, S. Goriely, T. Kondo, C. Iwamoto, H. Akimune, T. Yamagata, H. Toyokawa, H. Harada, F. Kitatani, Y.-W. Lui, A. C. Larsen, M. Guttormsen, P. E. Koehler, S. Hilaire, S. Péru, M. Martini, and A. J. Koning, Phys. Rev. C **88**, 015805 (2013).

[78] T. Nakamura, H. Sakurai, and H. Watanabe, Prog. Part. Nucl. Phys. **97**, 53 (2017).

[79] H. Watanabe, K. Yamaguchi, A. Odahara, T. Sumikama, S. Nishimura, K. Yoshinaga, Z. Li, Y. Miyashita, K. Sato, L. Próchniak, H. Baba, J. Berryman, N. Blasi, A. Bracco, F. Camera, J. Chiba, P. Doornenbal, S. Go, T. Hashimoto, S. Hayakawa, C. Hinke, N. Hinohara, E. Ideguchi, T. Isobe, Y. Ito, D. Jenkins, Y. Kawada, N. Kobayashi, Y. Kondo, R. Krücken, S. Kubono, G. Lorusso, T. Nakano, T. Nakatsukasa, M. Kurata-Nishimura, H. Ong, S. Ota, Z. Podolyák, H. Sakurai, H. Scheit, K. Steiger, D. Steppenbeck, K. Sugimoto, K. Tajiri, S. Takano, A. Takashima, T. Teranishi, Y. Wakabayashi, P. Walker, O. Wieland, and H. Yamaguchi, Phys. Lett. B **704**, 270 (2011).

[80] D. Doherty, J. Allmond, R. Janssens, W. Korten, S. Zhu, M. Zielińska, D. Radford, A. Ayangeakaa, B. Bucher, J. Batchelder, C. Beausang, C. Campbell, M. Carpenter, D. Cline, H. Crawford, H. David, J. Delaroche, C. Dickerson, P. Fallon, A. Galindo-Uribarri, F. Kondev, J. Harker, A. Hayes, M. Hendricks, P. Humby, M. Girod, C. Gross, M. Klintefjord, K. Kolos, G. Lane, T. Lauritsen, J. Libert, A. Macchiavelli, P. Napiorkowski, E. Padilla-Rodal, R. Pardo, W. Reviol, D. Sarantites, G. Savard, D. Seweryniak, J. Srebrny, R. Varner, R. Vondrasek, A. Wiens, E. Wilson, J. Wood, and C. Wu, Phys. Lett. B **766**, 334 (2017).

[81] C. L. Zhang, G. H. Bhat, W. Nazarewicz, J. A. Sheikh, and Y. Shi, Phys. Rev. C **92**, 034307 (2015).

[82] J. Skalski, S. Mizutori, and W. Nazarewicz, Nucl. Phys. A **617**, 282 (1997).

[83] S. Hilaire and M. Girod, Eur. Phys. J. A **33**, 237 (2007).

[84] K. Nomura, R. Rodríguez-Guzmán, and L. M. Robledo, Phys. Rev. C **94**, 044314 (2016).
[85] T. Togashi, Y. Tsunoda, T. Otsuka, and N. Shimizu, Phys. Rev. Lett. **117**, 172502 (2016).
[86] J. Zhao, B.-N. Lu, E.-G. Zhao, and S.-G. Zhou, Phys. Rev. C **95**, 014320 (2017).
[87] S. Miyahara and H. Nakada, Phys. Rev. C **98**, 064318 (2018).
[88] J. E. García-Ramos and K. Heyde, Phys. Rev. C **100**, 044315 (2019).
[89] D. Peña Arteaga, E. Khan, and P. Ring, Phys. Rev. C **79**, 034311 (2009).